

**ABSTRACT BOOKLET**

# 15. ANNUAL SCIENTIFIC SYMPOSIUM

Ultrahigh Field Magnetic Resonance: Clinical Needs,  
Research Promises and Technical Solutions

**September 13, 2024**

9:00 am - 6:00 pm

Max Delbrück Communications Center (MDC.C)

**MAX  
DELBRÜCK  
CENTER**

[www.mdc-berlin.de](http://www.mdc-berlin.de)

[www.mdc-berlin.de/MR\\_Symposium\\_2024](http://www.mdc-berlin.de/MR_Symposium_2024)

Max Delbrück Center for Molecular Medicine  
in the Helmholtz Association

Robert-Rössle-Straße 10, 13125 Berlin, Germany

# Message from the organizers

## Dear colleagues and friends,

Very warm welcome to Berlin. It is time to ride the wave of ultrahigh field MRI again. We are most of all excited by the larger audience that has joined us for the **15<sup>th</sup> Scientific Symposium on Clinical Needs, Research Promises and Technical Solutions in Ultrahigh Field Magnetic Resonance**.

Imaging bridges, a crucial gap in space and time in life science and medicine: from atomic to anatomic objects to whole body imaging, from picoseconds to years in population studies. New molecular and cellular insights are obtained from imaging. These findings should be integrated with data science into a coherent picture of tissues, organs and organisms for early interception of disease. These fundamental developments call for hitherto unavailable research frameworks, international partnership and collaborative culture to promote strong ties across multiple research domains and imaging modalities; connecting nanoscopic views, length scales, time scales and mesoscopic pictures with mechanistic insights and macroscopic function of biological and clinical importance. To meet this goal the Max Delbrück Center for Molecular Medicine; the Weizmann Institute of Science in Rehovot, Israel; the Humboldt University of Berlin and the Charité - Universitätsmedizin Berlin have established the Helmholtz International Research School (HIRS) on imaging and data science from the **NA**no to the **ME**so (*iNAMES*, <https://www.mdc-berlin.de/inames>) to intensify scientific interactions in imaging, data sciences, information technologies and digital engineering research fields.

The field of Magnetic Resonance (MR) has evolved rapidly over the past quarter of a century, allowing for an ever growing number of applications across a broad spectrum of basic, translational and clinical research. One important development which is in the spotlight of MR research is Ultrahigh Field Magnetic Resonance (UHF-MR). The pace of discovery is heartening and a powerful motivator to transfer the lessons learned at ultrahigh fields from basic research into the clinical scenario. These efforts are fueled by the unmet clinical needs and the quest for advancing the capabilities of diagnostic MR imaging – today.

The development of UHF-MR is moving forward at an amazing speed that is breaking through technical barriers almost as fast as they appear. UHF-MR has become an engine for innovation in experimental and clinical research. The reasons for moving UHF-MR into clinical applications are more compelling than ever. Images from these instruments have revealed new aspects of the anatomy, functions and

## Message from the organizers

physio-metabolic characteristics of the brain, heart, joints, kidneys, liver, eye, and other organs/tissues, at an unparalleled quality. UHF-MR has a staggering number of potential uses in neuroscience, neurology, radiology, neuroradiology, cardiology, internal medicine, oncology, nephrology, ophthalmology and other related clinical fields. As they are developed, we will push the boundaries of MR physics, biomedical engineering and biomedical sciences in many other ways.

With 7.0 T human MRI now widely used in clinical research, there is increasing interest in exploring even higher magnetic field strengths. This includes pioneering reports on MRI technology at 9.4 T, 10.5 T and 11.7 T and corresponding *in vivo* applications. The MR research and superconductor science community have already taken even more ambitious steps towards the future, envisioning human MR at 14.0 T. The Dutch National 14 Tesla Initiative in Medical Science is moving forward to the implementation of the first 14.0 T class human MR instrument. Joint efforts of the nuclear magnetic resonance (NMR) and MRI communities identified the scientific question that drives these ambitions, together with the technological challenges and prospects for achieving human MRI at 20.0 T. These bold steps will require rigorous technical developments, assessment of physiological constraints and *in vivo* evaluation studies, that have to be tested and validated by those who adopt the technology. The symposium offers ample opportunity for discussion and exchange on how such efforts can lead to valuable results.

Realizing these opportunities, we are very much delighted to very warm welcome you at the 15th Annual Scientific Symposium on Clinical Needs, Research Promises and Technical Solutions in Ultrahigh Field MR. The symposium is a collaboration between the Max Delbrück Center for Molecular Medicine, the Weizmann Institute of Science, the Charité Berlin, the German Metrology Institute (PTB) and the Hasso Plattner Institute. The symposium is designed to provide an overview of state-of-the-art (pre)clinical UHF-MR and its synergies with data science, and to initiate local, regional, national and international collaboration and last but not least to provide plenty of opportunities to engage into fruitful exchange with peers and colleagues.

For the scientific program we are very much honored to present extraordinary speakers including MR technology leaders, leading data scientists, distinguished clinical experts and emerging scientists – all bridging disciplinary boundaries and stimulating the imaging community to throw further weight behind the solution of unsolved

# Message from the organizers

problems and unmet clinical needs. The scientific program comprises 4 sessions, all balancing technical developments, clinical applications and hot topics related to the synergies between imaging and data science. The scientific program is designed to lay extensive bridges between disciplines to enable the translation of multimodal AI technology into clinically-relevant imaging guided diagnostics, therapy monitoring and digital health applications.

We would like to draw your attention to the posters, all being made readily available for viewing and downloading. We wish to thank those of you who walked the extra mileage and submitted poster contributions. We really appreciate your efforts. Thanks to your valuable feedback we have also included several slots of 3 min enlightening poster power presentations into the program. This will give a large number of poster presenters the opportunity to be in the spotlight of the audience. Please support the poster presenters and do not miss to vote for the best poster.

Last but not least we wish to thank the MDC's event team for their tremendous support.

We very warm welcome you to Berlin and to ultrahigh field MR



**Thoralf Niendorf**  
MDC & Charité, Berlin



**Lucio Frydman**  
Weizmann Institute of Science,  
Rehovot, Israel



**Jeanette Schulz-Menger**  
Charité, Berlin



**Christoph Lippert**  
HPI, Potsdam



**Michal Neeman**  
Weizmann Institute of  
Science, Rehovot, Israel



**Sonia Waiczies**  
MDC, Berlin



**Min-Chi Ku**  
MDC, Berlin



**Sebastian Schmitter**  
PTB, Berlin

# Grant Support

## The organizers wish to acknowledge the generous support provided by the Deutsche Forschungsgemeinschaft (DFG), the German Research Foundation

### About the DFG:

“The DFG is the self-governing organization for science and research in Germany. It serves all branches of science and the humanities. In organizational terms, the DFG is an association under private law. Its membership consists of German research universities, non-university research institutions, scientific associations and the Academies of Science and the Humanities.

The DFG supports projects from all scientific subject areas and especially promotes interdisciplinary cooperation between researchers. DFG funding enables cooperation between researchers from all branches of the science system as well as the formation of internationally conspicuous priorities at universities and non-university research institutions.

The foundation actively encourages international research cooperation: all of its programmes promote cooperation between scientists and academics in Germany and their colleagues abroad. It places special emphasis on collaboration in the scientific community in the European Research Area.

The DFG funds knowledge-oriented research and it welcomes and supports the cooperation of science with those who apply science in all areas of social life. This includes the interaction of scientific findings with industry and institutions like museums, academies of music, hospitals, and in public-private partnerships. Science and research are by definition international. Thus, the DFG’s statutes include an obligation to foster contacts between scientists and researchers in Germany and abroad.

To advance internationalization, the DFG has opened its funding programmes for international collaboration between researchers – an absolute necessity for Germany in its role as a pioneering and simultaneously cosmopolitan centre of research and science.”

For further details please visit: [www.dfg.de/en](http://www.dfg.de/en)

Funded by

**DFG**

Deutsche  
Forschungsgemeinschaft  
German Research Foundation

# Table of Contents

<b>Organization.....</b>	<b>04</b>
<b>Program .....</b>	<b>05</b>
<b>Poster Abstracts.....</b>	<b>09</b>
<b>Sponsors .....</b>	<b>46</b>



PRECLINICAL IMAGING

# Ultra-High Field MRI



Cutting-edge sensitivity and resolution

Highest commercially available preclinical MRI instruments with field strengths of 11.7 Tesla, 15.2 Tesla, and 18 Tesla.



For more information please visit [www.bruker.com](http://www.bruker.com)

Innovation with Integrity

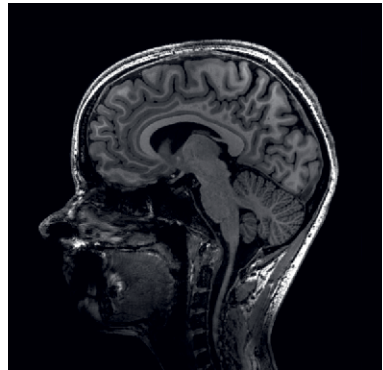
# MAGNETOM Terra.X

Make the difference.

[siemens-healthineers.com/terrax](https://www.siemens-healthineers.com/terrax)



MAGNETOM Terra.X\* introduces the next generation 7T MRI that will enable you to make the difference. With its groundbreaking Ultra IQ Technology, it will deliver unprecedented image clarity that allows you to confidently assess subtle pathological details. In combination with our AI-powered Deep Resolve, MAGNETOM Terra.X ultimately will take clinical routine to a new level. MAGNETOM Terra.X makes the difference for clinicians and scientists.



StudyID: 4aaaa0264 / 8Tx32Rx head coil

*\*MAGNETOM Terra.X is still under development and not commercially available yet. Its future availability cannot be ensured.*

# Organization

## **ORGANIZERS:**

<b>Thoralf Niendorf</b>	Berlin, Germany (MDC & Charité)
<b>Lucio Frydman</b>	Rehovot, Israel (Weizmann Institute of Science)
<b>Jeanette Schulz-Menger</b>	Berlin, Germany (Charité & Helios Klinikum)
<b>Michal Neeman</b>	Rehovot, Israel (Weizmann Institute of Science)
<b>Min-Chi Ku</b>	Berlin, Germany (MDC)
<b>Christoph Lippert</b>	Potsdam, Germany (HPI)
<b>Sebastian Schmitter</b>	Berlin, Germany (PTB)
<b>Sonia Waiczies</b>	Berlin, Germany (MDC)

## **CONFERENCE OFFICE:**

Lien-Georgina Dettmann, Matthias Runow & Timkehet Teffera  
E-Mail: [MRSymposium@mdc-berlin.de](mailto:MRSymposium@mdc-berlin.de)  
Max Delbrück Center for Molecular Medicine in the Helmholtz Association  
Robert-Rössle-Strasse 10  
13125 Berlin  
Phone: +49 30 9406 / 3720 / 2455 / 2719

## **OFFICE PROF. NIENDORF:**

Carolin Bechtloff: [Carolin.Bechtloff@mdc-berlin.de](mailto:Carolin.Bechtloff@mdc-berlin.de)  
Max Delbrück Center for Molecular Medicine in the Helmholtz Association  
Robert-Rössle-Straße 10  
13125 Berlin  
Phone: +49 30 9406 3978

# Program September 13, 2024

## 15<sup>TH</sup> ANNUAL SCIENTIFIC SYMPOSIUM ON ULTRAHIGH FIELD MAGNETIC RESONANCE

Friday, 13<sup>th</sup> September 2024

**09:00 WELCOME**

chair: Thoralf Niendorf, Berlin, Germany  
Sonia Waiczies, Berlin, Germany

### SCIENTIFIC SESSION I

#### GETTING TO THE MATTER OF THE HEART: CLINICAL NEEDS AND RESEARCH PROMISES OF CARDIOVASCULAR AND BODY UHF-MR

chair: Jutta Ellermann, Minneapolis, USA  
Thoralf Niendorf, Berlin, Germany

**09:10 Accelerated B1+ Mapping and Interleaved <sup>23</sup>Na/<sup>1</sup>H (pTx) MRI for Abdominal Imaging at 7T**

Judith Schirmer, Friedrich-Alexander-Universität, Erlangen, Germany

**09:30 It is all About Reproducibility: A 3-Year and an Inter-Day Study on the Robustness of Universal Excitation Pulses for Cardiac MRI at 7.0 T**

Manuel F Sánchez Alarcon, Physikalisch-Technische Bundesanstalt, Berlin, Germany

**09:50 Translational cardiovascular research: Cardiac MRI in Large Animal Models at 7.0 T.**

Alena Kollmann, University Hospital, Würzburg, Germany

**10:10 From Macrostructure to Microarchitecture: Comprehensive Cardiac MRI of Myocardial Reorganization in Hypertrophic Cardiomyopathy**

Oumaima Laghzali, Max Delbrück Center, Berlin, Germany

**10:30 POSTER POWER SESSION (3 x 3 min)**

**Hierarchical Self-Supervised Registration Pipeline for Enhancing Quantitative Cardiac MRI**

Xinqi Li, Biomedical Imaging Research Institute, Cedars-Sinai Medical Center, Los Angeles, USA

**Early Detection of Myocardial Strain Impairments in a Mouse Model of Hypertrophic Cardiomyopathy**

Siqin Liu, Max Delbrück Center, Berlin, Germany

**Monitoring Myocardial T2\* Transient Change in HCM: A Mouse Study**

Shahriar Shalika, Max Delbrück Center, Berlin, Germany

# Program September 13, 2024

**10:40** **PANEL DISCUSSION: CARDIAC AND BODY MRI at UH**

chair: Jutta Ellermann, Minneapolis, USA  
Christoph Aigner, Berlin, Germany

**10:55** **COFFEE BREAK / RELAXATION WITH LIVE MUSIC**

## SCIENTIFIC SESSION II

### GETTING TO THE MATTER OF THE BRAIN: CLINICAL NEEDS AND RESEARCH PROMISES FOR NEUROVASCULAR UHF-MR AND RELATED FIELDS

chair: Kamil Ugurbil, Minneapolis, USA  
Min-Chi Ku, Berlin, Germany

**11:15** **Functional 1H MRS and fMRI of the Brain to Decipher the Neurometabolite Response at 7.0 T**

Anouk Schranter, University Medical Center, Amsterdam, The Netherlands

**11:35** **Are Cortical Lesions an Early Hallmark of Multiple Sclerosis? The Answer is Provided by 7.0 T MRI**

Adil Maarouf, Aix-Marseille Université, Marseille, France

**11:55** **Precision fMRI at 7.0 T: How to Fix Cluster-Failure in the Individual Brain**

Igor F. Tellez Ceja, Max Delbrück Center, Berlin, Germany

**12:15** **High Accuracy Magnetic Field Shimming for Workflow Optimization: Methodology and Applications**

Hoby P. Hetherington, Resonance Research Incorporation, Billerica, USA

**12:35** **POSTER POWER SESSION (3 x 3 min)**

**Exploring the Topography of Metabolic Alterations in Multiple Sclerosis Using Fast High-Resolution 3D-MR Spectroscopic Imaging at 7.0 T**

Eva Niess, Medical University of Vienna, Austria

**Safety of Implanted Auditory Protheses at 7.0 T**

Guy Fierens, Cochlear Technology Centre, Mechelen, Belgium

**High Permittivity Dielectric Metasurfs Enhance Transmission Efficiency of a Surface Loop at 7.0 T**

Nandita Saha, Max Delbrück Center, Berlin, Germany

# Program September 13, 2024

**12:45** **PANEL DISCUSSION: BRAIN MRI at UHF**

chair: Sonia Waiczies, Berlin, Germany  
Assaf Tal, Rehovot, Israel

**13:00** **LUNCH BREAK / BREAKFAST BREAK**

## SCIENTIFIC SESSION III

### TRANSLATIONAL RESEARCH: FROM BLUE SKY EXPLORATIONS EN ROUTE TO CLINICAL APPLICATIONS

chair: Kamil Ugurbil, Minneapolis, USA  
Nandita Saha, Berlin, Germany

**13:45** **Sea to Summit: Progress in Preclinical MR at Ultrahigh and Extreme Magnetic Fields**

Wulf-Ingo Jung, Bruker Biospin MRI GmbH, Ettlingen, Germany

**14:05** **Of Possibilities and Pitfalls: Exploring Traces of Gadolinium Based Contrast Agents in the Kidney Using Mass Spectrometry and MRI**

Luis Hummel, Charité - Universitätsmedizin Berlin, Germany

**14:25** **Probing Myocardial Fibrosis and Scar Tissue with Quantitative MRI**

Elias Ylä-Herttua, University of Eastern Finland, Kuopio, Finland

**14:45** **Accelerated Simultaneous T2 and T2\* Mapping of the Brain and Beyond**

Jose Raul Velasquez Vides, Max Delbrück Center, Berlin, Germany

**15:05** **Can Hyperpolarization Add Value to Ultrahigh Field MRI?**

Shdema Epstein, NVision Imaging Technologies GmbH, Ulm, Germany

**15:25** **POSTER POWER SESSION (4 x 3 min)**

**Separation of Cellular ( $R_{2t}^*$ ), Vascular ( $R_{2'}$ ) and Macroscopic B0 Field Inhomogeneity (Background Gradients) Contributions to the  $R_{2}^*$  Signal Relaxation at UHF-MR**

Joanna Im, Mallinckrodt Institute of Radiology, Washington University, St. Louis, USA

**Characterization of Neuromuscular Organoids for Future Organoid MRI**

Lison Guillaume, Max Delbrück Center, Berlin, Germany

# Program September 13, 2024

## **Characterization of Fluorine MR Properties of the Multiple Sclerosis Drug Teriflunomide in Sweetened Milk**

Xiang Hu, Max Delbrück Center, Berlin, Germany

## **In Vivo Monitoring of Renal Tubule Volume Fraction During Acute Tubular Pressure Increase Using Dynamic T2 Mapping**

Ehsan Tasbihi, Max Delbrück Center, Berlin, Germany

### **15:35 PANEL DISCUSSION: TRANSLATIONAL MRI at UHF**

chair: Jason Millward, Berlin, Germany  
Sonia Waiczies, Berlin, Germany

### **15:50 COFFEE BREAK / RELAXATION WITH LIVE MUSIC**

## **SCIENTIFIC SESSION IV**

### **LOOKING AT THE HORIZON**

chair: Phil Selenko, Rehovot, Israel  
Bernd Ittermann, Berlin, Germany

### **16:15 Why all the Fuss About 7.0 T MRI? Smart Imaging of the Fetal Brain and Placenta at 0.55 T**

Jana Hutter, Friedrich-Alexander-Universität, Erlangen-Nürnberg, Germany

### **16:35 MRI at 10.5 T Matters**

Kamil Ugurbil, University of Minnesota, Minneapolis, USA

### **16:55 Beyond: 3D Metamaterial Facilitates Human Cardiac MRI at 21.0 T**

Bilguun Nurzed, Max Delbrück Center, Berlin, Germany

### **17:15 MRI at 5.0 T: Technology, Progress and Clinical Applications**

Benjamin Robert, United Imaging, Shanghai, PRC

### **17:35 Nova Terra: Progress in Clinical Ultrahigh Field MRI at 7.0 T**

Nicolas Behl, Siemens Healthineers, Erlangen, Germany

### **17:55 PANEL DISCUSSION: FUTURE of UHF MRI**

chair: Kamil Ugurbil, Minneapolis, USA  
Bernd Ittermann, Berlin, Germany

### **18:10 Get Together**

# Poster Abstracts

(In alphabetical order)



## Safety of Implanted Auditory Protheses at 7T

G. Fierens<sup>1</sup>, M. Clemence<sup>2</sup>, N. Verhaert<sup>3,4</sup>, R. Bowtell<sup>5,6</sup>, Rebecca S. Dewey<sup>5,6,7</sup>.

<sup>1</sup> Cochlear Technology Centre, Belgium,

<sup>2</sup> Philips Healthcare Clinical Science MR UK and Ireland, Farnborough, UK

<sup>3</sup> Research group Experimental Otorhinolaryngology, Department of Neurosciences, KU Leuven, Belgium,

<sup>4</sup> University Hospitals Leuven, Department of Otolaryngology, Head and Neck Surgery, Belgium

<sup>5</sup> Sir Peter Mansfield Imaging Centre, School of Physics and Astronomy, University of Nottingham, Nottingham, UK,

<sup>6</sup> National Institute for Health Research (NIHR) Nottingham Biomedical Research Centre, Nottingham, UK

<sup>7</sup> Hearing Sciences, Division of Mental Health and Clinical Neurosciences, School of Medicine, University of Nottingham, Nottingham, UK.

### Introduction

The use of magnetic resonance (MR) imaging and spectroscopy in patients with active implanted auditory protheses has become daily practice for diagnostic medical assessment. Many such protheses contain implanted retaining magnets that align the internal and external components of the device. Recently developed implants feature rotatable magnets, significantly improving the safety of MR scanning individuals using these implants at field strengths up to 3T. MR scanning of these people is conditionally approved by the international regulators, whereby the conditions imposed range from software limitation of the radiofrequency specific absorption rate (SAR) and gradient strength during scanning, to the removal of an implanted retaining magnet, if present. Failure to comply with these safety conditions carries the risk of damaging the implanted prosthesis, and/or causing pain and/or damage. Recently, scanners with a static magnetic field strength of 7T have become more widely available. Scanning implanted patients at ultra-high field strengths is likely to be associated with even greater risks for the patient. The aim of this study is to evaluate the safety of multiple active hearing implants in the 7T MR environment by assessing the mutual interactions occurring between the implantable device and the MR scanner and its environment.

### Methods

Several potential interactions were investigated using a 7T Philips Achieva MR scanner (Philips, Best, Netherlands), adhering to the relevant active industry standards. Measurements included: the magnetically induced force experienced by the implant housing and the implantable retaining magnet, demagnetisation of the implantable retaining magnet, electrical function of the implant following scanning, scanning-induced heating of the implant as caused by radiofrequency pulses and gradients, and quantification of image artefacts. Experiments were performed on three active

hearing implants: Nucleus type CI622 cochlear implant and Osia types OSI200 and OSI300 bone conduction implants (Cochlear Ltd., Sydney, AU).

## Results and discussion

Magnetically induced forces were measured by quantifying the deflection force when the device was suspended on a string close to the bore entry, where the spatial gradient field was maximal [2] (Fig. 2a). When no magnet was present, the force ratio defined as the magnetically induced force divided

by the force induced by gravity remained below 0.3 for all devices. With magnet in place, the force ratio increased up to 11 for the CI622 device.

Several implant magnets were exposed to the scanner's B0 field at body temperature, by bringing them into the MR environment up to isocentre, either with their main axis aligned with the field (N=12) or perpendicular to it (N=6). The magnetization of the magnets was measured before and after exposure using a magnetic field camera (Fig. 2b). In line with industry standards, a total of 10 exposures were performed [1]. Changes in magnetization were quantified per magnet and averaged for the population. Average magnetization changes of  $\pm 1\%$  were measured in both orientations, which is similar to the average population spread at baseline.

Device functionality after scanning was verified using the device fitting software (Fig. 2c). A dedicated experiment was performed for all devices where functionality was verified after a total of ten exposures, which according to industry standards [1] covers the need of 99.9% of the population. The same devices were used during all other tests afterwards, and intermediate functionality tests were performed.

Heating of the devices was measured using fiber-optic temperatures placed around the devices when placed in a liquid phantom at isocentre (RF) or 20 cm outside of isocentre (gradient) [1] (Fig. 2d). For all devices, heating remained limited to 0.15°C compared to background heating after 15 minutes consecutive scanning at 1 W/kg (RF-induced heating) or with a gradient field strength of 41.8 T/s (gradient-induced heating).

Image datasets were acquired with the device attached to the right side of the head of a commercial head phantom (Fig. 2e). A series of pulse sequences was selected based on the commonly used clinical examinations. Images were acquired in a coronal direction to limit scan time. When scanning with the magnet in place, the artefact covers almost the entire ipsilateral side of the head. When the magnet is replaced with the non-magnetic cassette, the extent of the artefact is notably reduced.

## Conclusion

This study documents the first results of a feasibility trial which investigated several interactions between active hearing implants and the ultra-high field 7T MR environment. Five interactions that may result in patient harm were assessed. These preliminary findings show no adverse effects on the implant within the predefined test conditions, and image artefacts similar to those seen at 3T.

Preliminary outcomes of this feasibility study are positive, yet do not imply implant safety in the 7T MR environment. Formal verification activities are required to label a device for use within the 7T MR environment.



**Figure 1**

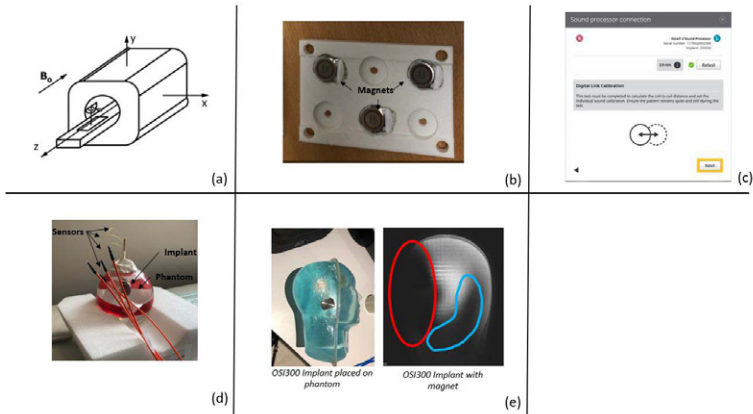


**Figure 2**

### Picture description

**Figure 1.** Prostheses being investigated: the Nucleus CI622 cochlear implant (left) and the Osia OSI200 and OSI300 bone conduction implants (middle and right, respectively)

**Figure 2.** Visual overview of performed tests: (a) magnetically induced force, according to ASTM F2052-21, (b) BO-induced demagnetisation, (c) implant functionality, (d) heating, and (e) implant-induced image artefacts

## Characterization of Neuromuscular organoids for future Organoid Magnetic Resonance Imaging

Lison Guillaume<sup>1,3</sup>, Thomas Gladytz<sup>1</sup>, Ines Lahmann<sup>1</sup>, Xiang Hu<sup>1,3</sup>, Helmar Waiczies<sup>1</sup>, Jason Millward<sup>1,2</sup>, Thoralf Niendorf<sup>1,2,3</sup>, Sonia Waiczies<sup>1,2</sup>

<sup>1</sup>Berlin Ultrahigh Field Facility (B.U.F.F.), Max Delbrück Center for Molecular Medicine in the Helmholtz Association, Berlin, Germany

<sup>2</sup>Experimental and Clinical Research Center (ECRC), A Joint Cooperation between the Charité Medical Faculty and the Max-Delbrück Center for Molecular Medicine in the Helmholtz Association, 13125 Berlin, Germany

<sup>3</sup>Charité-Universitätsmedizin Berlin, Germany

This preliminary study assessed the feasibility of MRI to image neuromuscular organoids (NMOs), which is a precursor to our future project studying fluorinated drugs in blood-brain-barrier (BBB) organoids[1]. Investigating drugs in this complex biological barrier is essential prior to animal investigations on selected test candidates [2]. The use of MRI on BBB organoids is crucial to bridge the gap between in vitro and in vivo studies, as it will allow far greater speed and flexibility to test drugs than is possible in animals, while using a system that is more physiologically relevant than cell culture. This strategy replaces the use of animals at this preliminary screening phase, and will greatly improve the success of subsequent animal experiments investigating fluorinated drugs in vivo. Fluorine-19 (19F) improves drugs potency and their cellular permeability and has the added advantage that these compounds can be detected by MR methods, as we previously reported in mice [3], [4].

We studied 100d old human NMOs produced using an SMAE1C4 iPSC line [5]. The NMOs were fixed in a solution of 4% paraformaldehyde diluted in phosphate buffered saline (PBS) for one hour. They were then washed twice with PBS then embedded in custom-made organoid chambers using 0.75% agarose in ddH<sub>2</sub>O. MR measurements were performed on a Bruker Biospec 9.4T pre-clinical MR scanner (Bruker BioSpin, Ettlingem Germany) equipped with a microimaging BG6 gradient (950mT/m, 80µs rise time) and a 1H mouse head coil. Longitudinal relaxation (T<sub>1</sub>) was measured using Flow-sensitive Alternating Inversion Recovery Rapid Acquisition with Relaxation Enhancement (FAIR RARE) mapping method (TR= 2654 ms, TE= 5 ms, exciting/reference flip angle= 90°/180°, spatial resolution=0.2mm, excitation pulse BW= 2000 Hz, FOV= 30x20 mm, slice= 0.6 mm, reference pow= 0.0669 W). All post-processing was performed with MATLAB R2019b.

NMOs (Figure 1A) fixed in agarose phantoms (Figure 1B,C) can be visualized using T<sub>1</sub> mapping (Figure 1D), in which different structures within the NMOs are observed, reflecting T<sub>1</sub> differences between the muscular (1) and neuronal (2) parts. The T<sub>1</sub>

for the muscular part (Figure 2.1) is  $2.269 \pm 0.064$ s (mean $\pm$ sd) and  $2.384 \pm 0.069$ s for the neuronal (Figure 2.2).

This preliminary study demonstrates that different tissue types in organoids can be distinguished based on their T1 relaxation times. These findings are promising for deepening our research on drug distribution in BBB organoids.

## References

- [1] S. Bergmann et al., "Blood-brain-barrier organoids for investigating the permeability of CNS therapeutics," *Nat Protoc*, vol. 13, no. 12, pp. 2827–2843, Dec. 2018, doi: 10.1038/s41596-018-0066-x.
- [2] A. Gregson, K. Thompson, S. E. Tsirka, and D. L. Selwood, "Emerging small-molecule treatments for multiple sclerosis: Focus on B cells.," 2019, F1000 Research Ltd. doi: 10.12688/f1000research.16495.1.
- [3] Y. Pan, "The dark side of fluorine," *ACS Med Chem Lett*, vol. 10, no. 7, pp. 1016–1019, Jun. 2019, doi: 10.1021/acsmchemlett.9b00235.
- [4] L. Starke et al., "First in vivo fluorine-19 magnetic resonance imaging of the multiple sclerosis drug siponimod," *Theranostics*, vol. 13, no. 4, pp. 1217–1234, 2023, doi: 10.7150/thno.77041.
- [5] A. Urzi et al., "Efficient generation of a self-organizing neuromuscular junction model from human pluripotent stem cells," *Nat Commun*, vol. 14, no. 1, Dec. 2023, doi: 10.1038/s41467-023-43781-3.

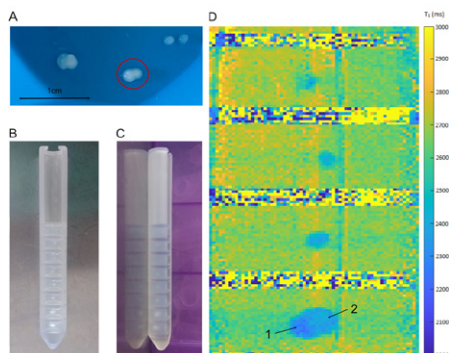


**Figure 1**

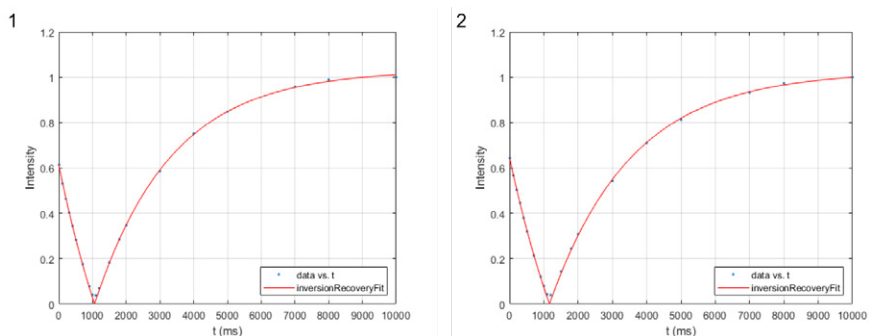


**Figure 2**

**Picture description**

**Figure 1:** T1 mapping and setup of the MRI of organoids (A) NMOs used in the organoid chamber; NMO used in Figure 2 is circled in red (B) organoid chamber front view (C) organoid chamber side view (D) T1 mapping of four neuromuscular organoids (NMOs) of different sizes including the NMO studied through inversion recovery T1 with 1: muscular part of the NMO; 2: neuronal part of the NMO.

**Figure 2:** Partial inversion recovery T1 fitting of (1 from figure 1D) the muscular part of the neuromuscular organoids (NMO) (2) the neuronal part of the NMO.

## Characterization of Fluorine MR Properties of the Multiple Sclerosis Drug Teriflunomide in Sweetened Milk

Xiang Hu<sup>1,2,3</sup>, Nandita Saha<sup>1,2,3</sup>, Yinhao Chen<sup>1</sup>, Jason M. Millward<sup>1,2</sup>, Christian Prinz<sup>4</sup>, Ludger Starke<sup>1</sup>, Lison Neige Guillaume<sup>1</sup>, Helmar Waiczies<sup>1</sup>, Marc Nazaré<sup>5</sup>, Michael Rothe<sup>6</sup>, Friedemann Paul<sup>2,3</sup>, Thoralf Niendorf<sup>1,2,3</sup>, and Sonia Waiczies<sup>1,2</sup>

<sup>1</sup>Berlin Ultrahigh Field Facility (B.U.F.F.), Max Delbrück Center for Molecular Medicine in the Helmholtz Association, Berlin, Germany

<sup>2</sup>Experimental and Clinical Research Center (ECRC), A Joint Cooperation between the Charité Medical Faculty and the Max-Delbrück Center for Molecular Medicine in the Helmholtz Association, Berlin, Germany

<sup>3</sup>Charité-Universitätsmedizin Berlin, Germany

<sup>4</sup>SRH Fernhochschule – The Mobile University, Riedlingen, Germany

<sup>5</sup>Medicinal Chemistry, Leibniz-Institut für Molekulare Pharmakologie (FMP), Berlin, Germany

<sup>6</sup>Lipidomix GmbH, Berlin, Germany

### Introduction

Teriflunomide (TF) is a multiple sclerosis (MS) drug. Like other fluorinated drugs, could be detected in vivo with <sup>19</sup>F MR methods, as shown in the MS animal model, experimental autoimmune encephalomyelitis (EAE)[1-4]. In the EAE, we administer drugs in sweetened milk (SM) or sucrose to facilitate voluntary oral application. Since it is unclear whether these drug delivery vehicles could alter the physicochemical properties of the drugs. We conducted phantom experiments, TF was dispersed in different vehicles (DMSO, DMSO+SM, CMC, CMC+SM and serum), to study the <sup>19</sup>F MR properties change. The goal is to evaluate the suitability of SM as a potential drug delivery vehicle for theranostic applications in mice.

### Methods

For phantom preparation, TF was dispersed in DMSO, DMSO+SM, CMC, CMC+SM and serum. Phantom experiments were performed using a Bruker 9.4T pre-clinical MR scanner maintaining physiological temperatures (PT) with water-bath circulation throughout the entire process. Longitudinal relaxation time ( $T_1$ ) measurements were done with the single-pulse <sup>19</sup>F MRS FID sequence with 23 different TRs (100 – 10000 ms). Transverse relaxation time ( $T_2$ ) measurements were done with a CPMG sequence with 25 different TEs[Sww2] (2 – 1000 ms). Then estimated  $T_1$  and  $T_2$  by fitting the  $T_1$  and  $T_2$  relaxations equations to the measured <sup>19</sup>F signal intensities[4] and determined the  $R^2$  (coefficient of determination) to show the goodness of fit. All post-processing was in MATLAB R2021b.

## Results

All  $^{19}\text{F}$  spectrums of TF showed a single peak at  $-57.9$  ppm ( $\text{TF}_{\text{DMSO}}$  and  $\text{TF}_{\text{DMSO+SM}}$ ),  $-61.1$  ppm ( $\text{TF}_{\text{CMC}}$  and  $\text{TF}_{\text{CMC+SM}}$ ) and  $-60.9$  ppm ( $\text{TF}_{\text{serum}}$ ) (Fig.1 A-E). All  $T_1$  relaxations were similar at c.1000 ms (Fig.1F-J). However, SM reduced the  $T_2$  of  $\text{TF}_{\text{DMSO}}$  from 326 ms to 186 ms ( $\text{TF}_{\text{DMSO+SM}}$ ) (Fig.1K and L).  $T_2$  of  $\text{TF}_{\text{CMC}}$  was also reduced while the addition of SM, from 251 ms to 2 ms ( $\text{TF}_{\text{CMC+SM}}$ ) (Fig.1M and N). The  $T_2$  of  $\text{TF}_{\text{CMC+SM}}$  (Fig.1N) is comparable to  $\text{TF}_{\text{serum}}$  (Fig.1O).

## Conclusion

Our results show that sweetened milk alters the  $^{19}\text{F}$  MR properties of TF suggesting that milk protein might be interacting with TF on a molecular level, consistent with earlier studies showing the same phenomena with serum protein[2,3]. In addition to assessing its theranostic properties, we are currently conducting pharmacological tests to evaluate the inhibitory effects of TF in the presence of sweetened milk. These tests aim to explore potential influences on its therapeutic efficacy in voluntary treatments in mice, when using sweetened milk.

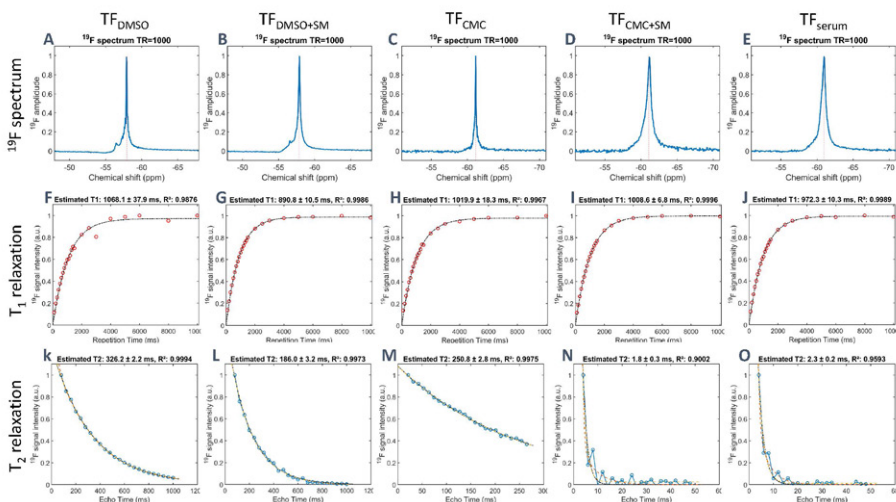


**Figure 1:**  $^{19}\text{F}$  MR properties of TF in different vehicles. (A-E)  $^{19}\text{F}$  MR spectrum of TF in different vehicles (TR = 1000 ms). (F-J)  $T_1$  relaxation of TF in different vehicles. (K-O)  $T_2$  relaxation of TF in different vehicles.

## Separation of Cellular ( $R2t^*$ ), Vascular ( $R2'$ ), and Macroscopic $B_0$ Field Inhomogeneity (Background Gradients) Contributions to the $R2^*$ Signal Relaxation at Ultra-High Fields with quantitative Gradient Recalled Echo (qGRE) MRI

Joanna Im, Victoria Levasseur, Biao Xiang, Alexander L. Sukstanskii, James D. Quirk, Satya V.V.N. Kothapalli, Anne H. Cross, and Dmitriy A. Yablonskiy\*.

Mallinckrodt Institute of Radiology, Washington University in St. Louis

\* Corresponding author: yablonskiyd@wustl.edu

Ultra-High Field (UHF)  $R2^*$  relaxometry is becoming increasingly popular for in vivo high-resolution analysis of biological tissue cellular microstructure and neuropathology with MRI. However, most researchers apply data analysis that equate transverse relaxation rate parameter  $R2^*$  of MRI signal to the tissue microstructure without accounting for vascular contributions to  $R2^*$  signal, i.e. the Blood-Oxygen-Level Dependent (BOLD) signal component, and magnetic field inhomogeneities. These effects are especially important at UHF as their contribution to  $R2^*$  scales linearly with magnetic field. Hence, vascular component needs to be separated from  $R2^*$  to obtain accurate information on tissue microstructure. Thus, an effective method to separate  $R2^*$  components become crucial to provide a non-invasive, accurate diagnostic tool for neuropathology.

Our study aims to create a procedure to accurately separate  $R2t^*$  (tissue-specific sub-component),  $R2'$  (vascular BOLD component), and contributions from the adverse effects of magnetic field inhomogeneities from the total  $R2^*$  signal at UHF MRI.

Four healthy, 8-week-old C57BL/6J mice were imaged in vivo with multigradient echo MRI at 9.4T field strength and analyzed using the quantitative Gradient Recalled Echo (qGRE) MRI approach (1). A segmentation protocol was established using the Dorr Mouse Brain Atlas and ANTs Syn registration to warp template brain region labels to subject qGRE maps for region-specific  $R2^*$  analysis within grey matter labels. Our findings reveal significant contributions of  $R2'$  to  $R2^*$ , with approximately 42% of the  $R2^*$  signal arising from vascular contributions.

Our results suggest the advantages of the qGRE approach and signal separation in comparison to  $R2^*$  mapping in high-field MRI studies of brain tissue microstructure in health and disease.

### Reference

- (1) Ulrich and Yablonskiy, *Separation of cellular and BOLD contributions to  $T2^*$  signal relaxation*. Magnetic resonance in medicine, 2016. **75**: p. 606-615).

# Hierarchical Self-Supervised Registration Pipeline for Enhancing Quantitative Cardiac MRI

Xinqi Li<sup>1,2</sup>, Li-ting Huang<sup>2</sup>, Thoralf Niendorf<sup>1</sup>, Min-chi Ku<sup>1</sup>, and Hsin-Jung Yang<sup>2</sup>

<sup>1</sup>Berlin Ultrahigh Field Facility (B.U.F.F.), Max Delbrück Center for Molecular Medicine in the Helmholtz Association (MDC), Berlin, Germany

<sup>2</sup>Biomedical Imaging Research Institute, Cedars-Sinai Medical Center, Los Angeles, CA, United States

## Introduction

Quantitative cardiac MRI (CMR) is an increasingly important tool for cardiovascular diagnosis. Traditionally, Late Gadolinium Enhancement (LGE) serves as the reference standard for identifying myocardial scar and focal fibrosis, whereas the diffuse fibrosis might not be detected<sup>1</sup>. Extracellular volume fraction (ECV) is a quantitative CMR mapping technique that captures both focal and diffuse alternations in myocardium structure by utilizing the contrast-enhanced T1 mapping (post-contrast T1) and native T1 mapping (pre-contrast T1) to calculate the ECV fraction. However, the respiratory and cardiac motion during the CMR acquisition can adversely degrade the quality of the quantitative mapping, leading to tissue misalignment across images and reducing the accuracy of the final mapping. Therefore, effective co-registration among both inter- and intra-sequence images is a crucial requirement of the post-processing pipeline to enhance mapping quality.

We propose a hierarchical self-supervised registration pipeline building upon our previous work. Our contrast-agnostic groupwise registration model rPCA-GroupRegNet<sup>2</sup> robustly registers images despite contrast variations. By leveraging the intra-scan motion-corrected images from the first-level registration to guide the second level, we ensure that misalignment between pre-contrast and post-contrast will be corrected through the registration of average reference, thereby enhancing the accuracy and reliability of ECV mapping.

## Methods

The pipeline included two-level registration as shown in Fig.1. The rPCA-GroupRegNet for the first level corresponding pre-contrast and post-contrast images  $I_N^{\text{pre}} = \{I_i \in \mathbb{R}^{H \times W} | i=1 \dots N\}$  and  $I_N^{\text{post}} = \{I_i \in \mathbb{R}^{H \times W} | i=1 \dots N\}$  were registered independently. This registration generated the deformation field  $D_N^{\text{pre}} = \{D_i \in \mathbb{R}^{2 \times H \times W} | i=1 \dots N\}$  and  $D_N^{\text{post}} = \{D_i \in \mathbb{R}^{2 \times H \times W} | i=1 \dots N\}$  and warped images  $D_N^{\text{pre}} \circ I_N^{\text{pre}}$ ,  $D_N^{\text{post}} \circ I_N^{\text{post}}$  accordingly.

For the second level, the input of the model  $X = \{X_i \in \mathbb{R}^{H \times W} | i=1, 2\}$  was the concatenated  $I_{\text{avg}}^{\text{pre}}$  and  $I_{\text{avg}}^{\text{post}}$ , where the pixel-wise average reference was generated by

$$I_{\text{avg}} = 1/N \sum (D_n \circ I_n).$$

The model generated the deformation field  $\varphi_n$ , including  $\varphi_{pre}$  and  $\varphi_{post}$ . The warped images of the second level were generated by

$$I_{reg}^i = (D_n + \varphi_n) \circ I_n,$$

where deformation fields from two levels were added and applied to the original weighted images. These warped images were used to calculate the registered T1 map and ECV mapping using the definition:

$$ECV = (1 - \text{haematocrit}) \times (1/T1_{Myo}^{post} - 1/T1_{Myo}^{pre}) / (1/T1_{Blood}^{post} - 1/T1_{Blood}^{pre}),$$

where haematocrit represents the cellular fraction of blood.

## Results

We tested the pipeline on pre-contrast and 15-minute post-contrast T1-weighted images and T1 maps from three patient subjects with Fabry’s disease. The representative images from 1 patient are shown in Fig. 2. The observed misalignment (white arrows) between the pre- and post-contrast T1 maps resulted in ECV maps with extraneous artifacts, which might lead to potential distortions in the quantification of extracellular volume. However, our hierarchical registration model effectively corrected both intra-subject and inter-subject motion (green arrows). To quantitatively assess the accuracy of the registration, we manually delineated the myocardium contours on both pre- and post-contrast T1 maps and computed the Dice similarity coefficient as illustrated in Fig. 3. The average Dice scores across the test subjects were 0.21 for the original images, 0.27 after the first level of registration, and 0.76 after the second level of registration.

## Conclusion

Our proposed hierarchical self-supervised registration pipeline has demonstrated substantial potential in addressing both inter- and intra-sequence motion, thereby improving the quality of the quantitative mapping, such as ECV mapping. This improvement ensures more reliable imaging data, paving the way for better diagnostic precision in cardiovascular diseases. In the future, we plan to incorporate the physical information to enhance the registration further and explore other quantitative mappings such as DCE mapping.

## References

1. P. Haaf, P. Garg, D. R. Messroghli, D. A. Broadbent, J. P. Greenwood, and S. Plein, “Cardiac T1 Mapping and Extracellular Volume (ECV) in clinical practice: a comprehensive review,” *J. Cardiovasc. Magn. Reson.*, vol. 18, no. 1, p. 89, Nov. 2016, doi: 10.1186/s12968-016-0308-4.
2. X. Li, Y. Zhang, Y. Zhao, J. van Gemert, and Q. Tao, “Contrast-Agnostic Groupwise Registration by Robust PCA for Quantitative Cardiac MRI,” in *Statistical Atlases and Computational Models of the Heart. Regular and CMRxRecon Challenge Papers*, O. Camara, E. Puyol-Antón, M. Sermesant, A. Suinesiaputra, Q. Tao, C. Wang, and A. Young, Eds., Cham: Springer Nature Switzerland, 2024, pp. 77–87

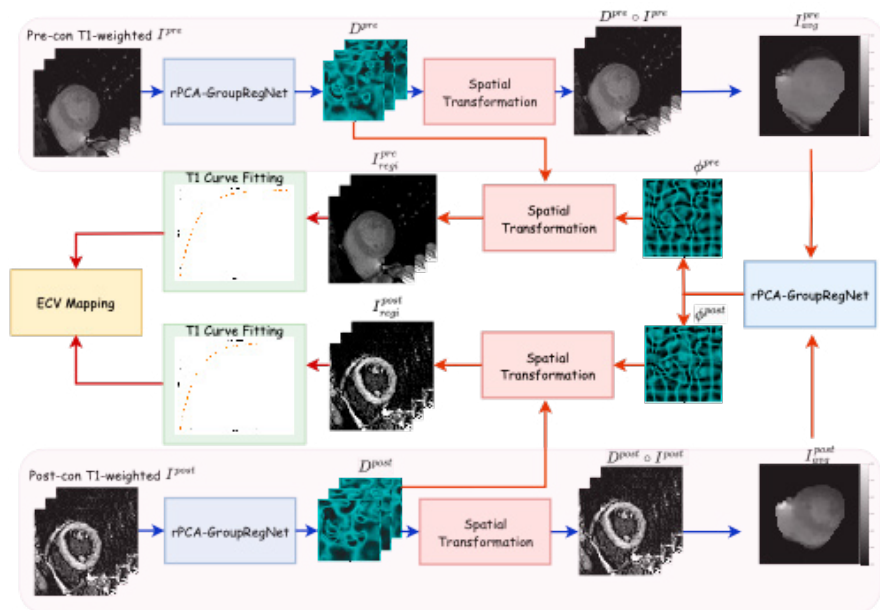


Figure 1

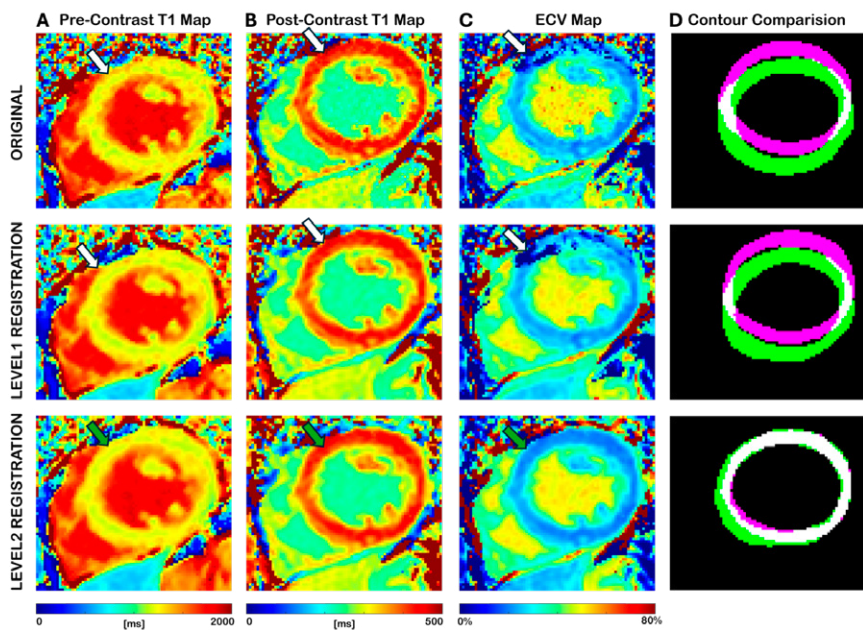


Figure 2

### Picture description

**Figure 1:** Proposed framework for hierarchical self-supervised registration to ensure accurate data alignment. The blue arrows indicate the first level registration and red arrows indicate the second level registration.

**Figure 2:** The comparison of pre-, post-contrast T1 map and ECV map between original, level1 registration and proposed level2 registration. Column A, B and C are the corresponding pre-contrast, post-contrast T1 map and ECV map and column D shows overlapping comparison of myocardium mask between pre- and post-contrast T1 map. The green mask indicates the pre-contrast T1 map and pink mask indicates the post-contrast T1 map's myocardium region. The white region indicates the overlapped region between two masks. The misalignment between pre-contrast and post-contrast T1 map was severe for original and single level registration, which introducing artefacts into ECV maps (white arrows). The proposed hierarchical registration (bottom row) calibrated the maps and improve the quality of the ECV map (green arrows).

## Early Detection of myocardial strain impairments in a mouse model of hypertrophic cardiomyopathy

*Siqin Liu<sup>1,2,3</sup>, Oumaima Laghzali<sup>1,2,3</sup>, Shahriar Shalikar<sup>1</sup>, Lucie Carrier<sup>5,6</sup>, Thoralf Niendorf<sup>1,2,3,4</sup>, Min-Chi Ku<sup>1,2</sup>*

<sup>1</sup>Berlin Ultrahigh Field Facility (B.U.F.F.), Max Delbrück Center for Molecular Medicine in the Helmholtz Association, Berlin, Germany;

<sup>2</sup>DZHK (German Centre for Cardiovascular Research), partner site Berlin, Germany;

<sup>3</sup>Charité-Universitätsmedizin Berlin, Berlin, Germany;

<sup>4</sup>Experimental and Clinical Research Center, Charite Medical Faculty and the Max Delbrueck Center for Molecular Medicine in the Helmholtz Association, Berlin, Germany;

<sup>5</sup>Department of Experimental Pharmacology and Toxicology, University Medical Center Hamburg-Eppendorf, Germany;

<sup>6</sup>German Center for Cardiovascular Research-Partner Site Hamburg/Kiel/Luebeck

### Introduction

Hypertrophic cardiomyopathy (HCM), affecting 1:200-500 people, is the most common inherited cardiac condition, characterized by hypertrophy and hypercontractility(1). Traditional metrics like ejection fraction and fractional shortening inadequately assess subtle myocardial deformations(2). Myocardial strain measurement offers superior detection of early dysfunction, regional variations, and excessive contraction in HCM(3). This study employs cardiac magnetic resonance with feature tracking (CMR-FT) to assess global and regional myocardial strain in both left and right ventricles of an HCM mouse model, seeking to identify early imaging markers.

### Methods

We utilized a HCM model (Mybpc3-KI) which carries a point mutation in the Mybpc3 gene on a C57BL/6 background. The level of total cMyBP-C mRNA was reduced by 50% in heterozygotes (HET) representing early-phase HCM and by 80% in homozygotes (KI) representing severe HCM(4). In total, 62 mice (31 male and 31 female; includes 20 WT, 28 HET and 14 KI) underwent CINE-CMR for functional and feature tracking based strain assessment at 9.4T. Cardiac short-axis (SAX) views were captured with 7-8 slices per heart. Left ventricular (LV) wall thickness was measured in end-diastole. Cardiac function and strain (LV and RV strain and strain rate) were analysed using Segment Version 4.0 (Medviso, Lund, Sweden), with endo- and epicardial borders manually delineated at end-systole and end-diastole from SAX and long-axis (LAX) CINE images (four chamber view).

## Results

The study of 62 mice revealed significant differences in ventricular function between wild-type (WT), KI, and HET groups. KI mice exhibited lower ejection fractions and hypertrophy compared to WT, while HET mice retain normal. CMR-FT analysis demonstrated that KI mice had significantly reduced global strain values in LV and RV and lower strain rates across all dimensions. Notably, torsion and LV systolic longitudinal strain rate (LVSLST) showed significant differences between WT and HET mice, particularly in females, suggesting their potential as early markers for HCM. Our analysis of 20 young mice (7-8 weeks old) revealed significant differences in left ventricular torsion and systolic longitudinal strain rate (LVSLST), particularly pronounced in females. These findings strongly support the potential of torsion and LVSLST as early imaging biomarkers for HCM detection. The age-specific results underscore the sensitivity of these parameters in identifying subtle cardiac changes before overt disease manifestation, highlighting their promise for early HCM diagnosis.

## Conclusions

Our study identified ventricular mechanical dysfunctions in HCM using CMR feature tracking, confirming torsion and LVGLST as potential early imaging markers of HCM.

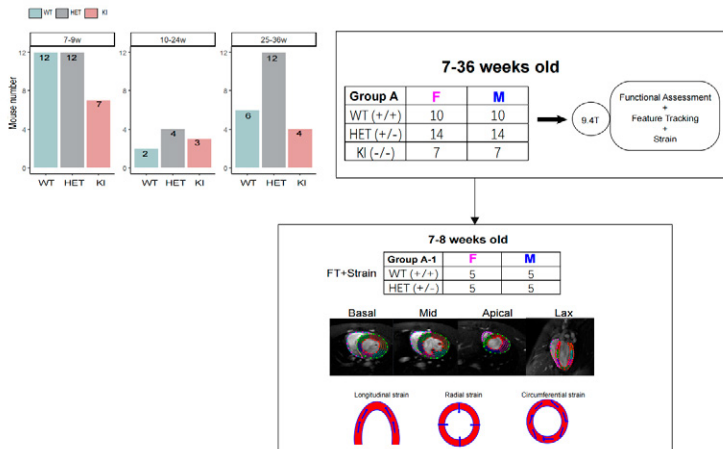
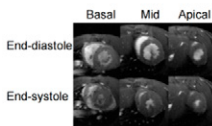
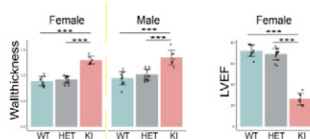


Figure 1

a. Representative FLASH cine images



b. LV thickness



c. Ejection Fraction

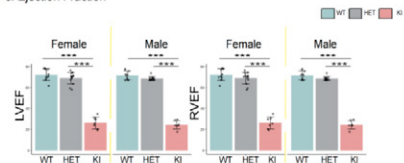
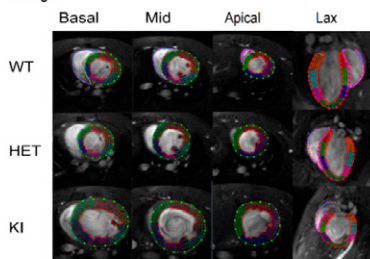
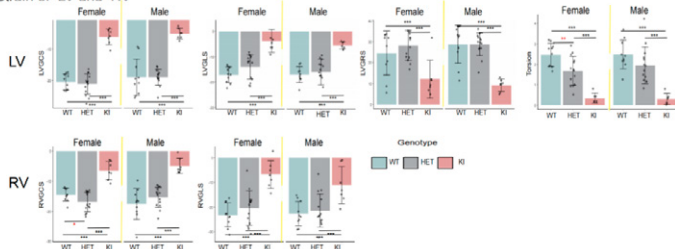


Figure 2

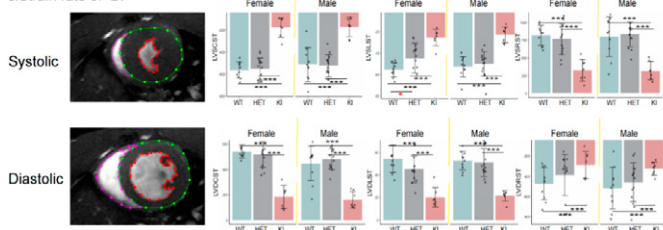
a. FT image



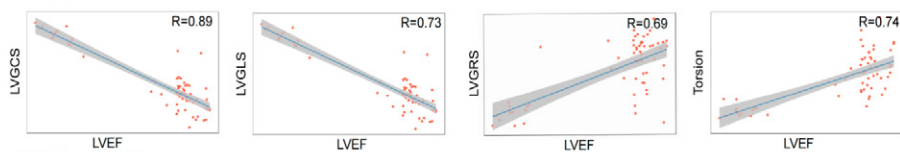
b. Strain of LV and RV



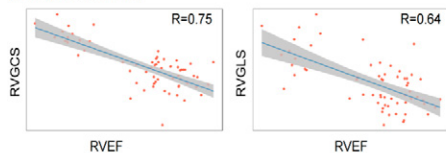
c. Strain rate of LV



d. LV strain and LVEF



e. RV strain and RVEF



f. LV strain and RV strain

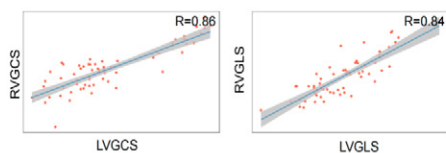
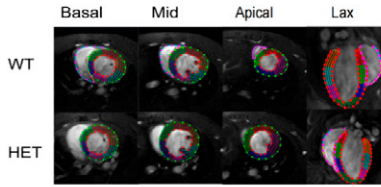
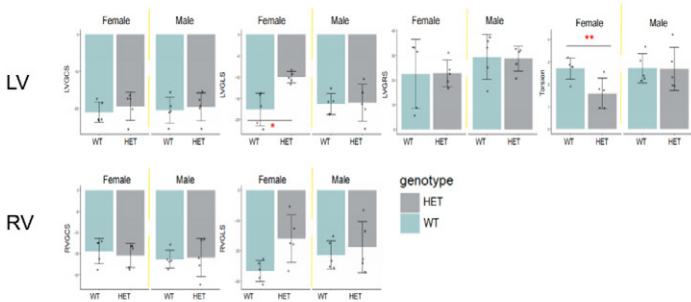


Figure 3

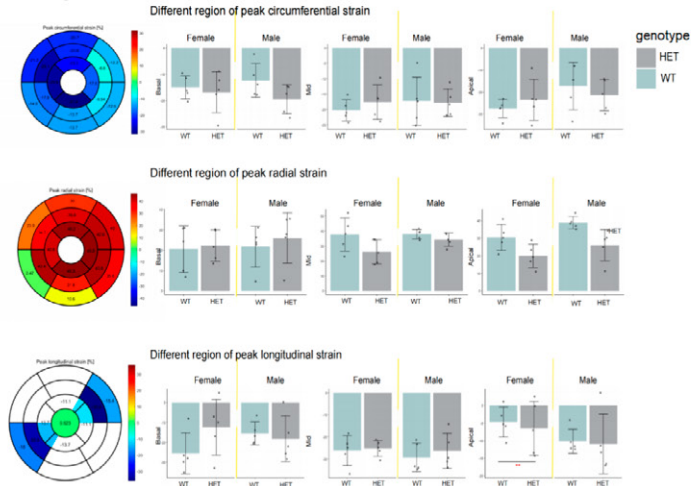
a. FT image



b. Strain of LV



c. Different region of LV



d. LV Strain and RV strain of different gender

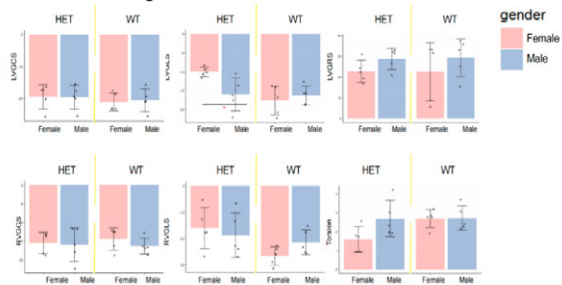


Figure 4

## Picture description

**Figure 1:** schematic depiction of the study design. Following genotyping, all mice underwent MRI as illustrated, followed by strain analysis in mice aged 7-8 weeks from both wild-type (WT) and heterozygous (HET) groups. Strain is categorized into different directions during systole, reflecting longitudinal and circumferential shortening, as well as radial thickening.

**Figure 2:** Functional Analysis of Ventricular Performance in Mice with Different Genotypes and Genders Using Cine-CMR Imaging. a. Endocardial and epicardial borders were manually segmented for end-systole and end-diastole using a stack of short-axis FLASH cine images in both male and female mice. b. Left ventricular (LV) thickness was presented as mean values with standard deviation (SD) on a slice-by-slice basis. c. Functional assessment, including left ventricular ejection fraction (LVEF) and right ventricular ejection fraction (RVEF), was presented as mean values with standard deviation (SD).

**Figure 3:** Myocardial Strain Variations in LV and RV of Mice with Different Genotypes and Genders Obtained from CMR Feature Tracking. a. FT images displayed at different slices for different genotypes. b. LV strain assessments (including LV global circumferential strain (LVGCS), LV global radial strain (LVGRS), LV global longitudinal strain (LVGLS), and torsion) and RV strain assessments (including RV global circumferential strain (RVGCS) and RV global longitudinal strain (RVGLS)) were presented as mean values with standard deviation (SD) on a slice-by-slice basis. Significance levels are indicated as \* $p < 0.05$  and determined using one-way ANOVA with Tukey's test. c. LV strain rate assessments, including LV global diastolic/systolic circumferential strain rate (LVDCST/LVSCST), LV global diastolic/systolic radial strain rate (LVDRST/LVSRST), and LV global diastolic/systolic longitudinal strain rate (LVDLST/LVSLST), were presented as mean values with standard deviation (SD) on a slice-by-slice basis. d. Correlation between LV strain (LVGCS, LVGRS, LVGLS, Torsion) and LVEF. e. Correlation between RV strain (RVGCS and RVGLS) and RVEF. Linear regression analyses were performed to assess the relationship between strain and ejection fraction. f. Linear regression analyses were performed to assess the relationship between LV strain and RV strain. The strength of the correlation coefficient ( $r$ ) in linear regression analyses was interpreted as strong:  $r > 0.7$ ; moderate:  $0.3 < r < 0.7$ ; weak:  $r < 0.3$ . Significance levels are indicated as \* $p < 0.05$  and \*\*\* $p < 0.01$ , determined using one-way ANOVA with Tukey's test.

**Figure 4:** Myocardial Strain Variations in LV and RV of Mice between 7 and 8 weeks old Obtained from CMR Feature Tracking (FT). a. FT images displayed at different slices for WT and HET mice between 7 and 8 weeks old. LV strain assessments (including LVGCS, LVGRS, LVGLS, and torsion) and RV strain assessments (including RVGCS and RVGLS) were conducted on the cine images above. b. Different genotype of various strain assessments (including LV and RV strain) were presented as mean values with standard deviation (SD) on a slice-by-slice basis. c. Different region of various strain assessments (including peak circumferential strain, peak radial strain, and peak longitudinal strain) were also evaluated. d. Different gender of various strain assessments (including LV and RV strain) were assessed. Mean values with standard deviation (SD) were presented. Significance levels are indicated as \* $p < 0.05$  and determined using one-way ANOVA with Tukey's test.

## Exploring the topography of metabolic alterations in multiple sclerosis using fast high-resolution 3D-MR spectroscopic imaging at 7T

Eva Niess<sup>1</sup>, Assunta Dal-Bianco<sup>2</sup>, Fabian Niess<sup>1</sup>, Bernhard Strasser<sup>1</sup>, Lukas Hingerl<sup>1</sup>, Wolfgang Bogner<sup>1,3</sup>

<sup>1</sup> High-Field MR Center, Department of Biomedical Imaging and Image-guided Therapy, Medical University of Vienna, Vienna, Austria

<sup>2</sup> Department of Neurology, Medical University of Vienna, Vienna, Austria

<sup>3</sup> Christian Doppler Laboratory for MR Imaging Biomarkers (BIOMAK), Department of Biomedical Imaging and Image-guided Therapy, Medical University of Vienna, Vienna, Austria

### Objectives

To explore the extent and topography of brain metabolic abnormalities of multiple sclerosis (MS) we utilised echo-less 3D-MR spectroscopic imaging (MRSI) at 7T.

### Methods

We included 26 MS patients (13 women, 13 men; median age 34 years) and 13 age- and sex-matched healthy controls (7 women, 6 men; median age 33 years) in this study. Participants underwent 3D-MRSI with concentric rings trajectory readout at 7T with an acquisition delay/TR of 1.3/320ms, 64×64×33 matrix, 3.4×3.4×4 mm<sup>3</sup> nominal voxel volume in 8:20 minutes. Metabolic maps of myo-inositol (mI), N-acetylaspartate (NAA), total choline (tCho), total creatine (tCr) and glutamate (Glu) were obtained. After spatial normalisation to study-specific atlas space, patients' and controls' maps were compared using permutation interference *randomise* of FSL to determine the topography of metabolic abnormalities and their associations with clinical disability status as measured with Expanded Disability Status Scale (EDSS) score.

### Results

Sample metabolic maps of one MS patient and age-matched control are depicted in *Figure 1*. Voxel-wise analysis (FSL *randomise* non-parametric permutation testing,  $P < 0.05$ , threshold-free cluster enhancement and family-wise error multiple comparison correction, age and sex as confounding covariate) identified clusters of elevated mI/tCr in bilateral cerebral white matter (WM) (*Figure 2A*) and cluster of reduced NAA/tCr in bilateral cerebral WM, bilateral superior frontal WM, right paracentral WM and left superior frontal cortex (*Figure 2B*). Within the significant clusters mI/tCr levels were  $1.35 \pm 0.13$  for MS and  $1.15 \pm 0.10$  for controls. The NAA/tCr levels within the significant clusters were  $1.40 \pm 0.10$  for MS and  $1.62 \pm 0.12$  for controls.

Clusters of metabolic abnormalities were co-localised with lesion probability maps, in particular NAA/tCr (*Figure 2C*), but were also observed dominantly in the superior frontal- and parietal normal-appearing WM which were spared from lesional pathology. Positive correlations between mI/NAA and clinical disability score (EDSS) were found in bilateral cerebral and superior frontal WM ( $r=0.45$ ,  $P=0.022$ ) (*Figure 3*).

## Conclusions

The study mapped metabolic abnormalities associated with MS, providing insights into the topography of their related pathological processes (neuronal damage = reduced NAA and neuroinflammation-induced gliosis = increased mI) and their clinical impact.

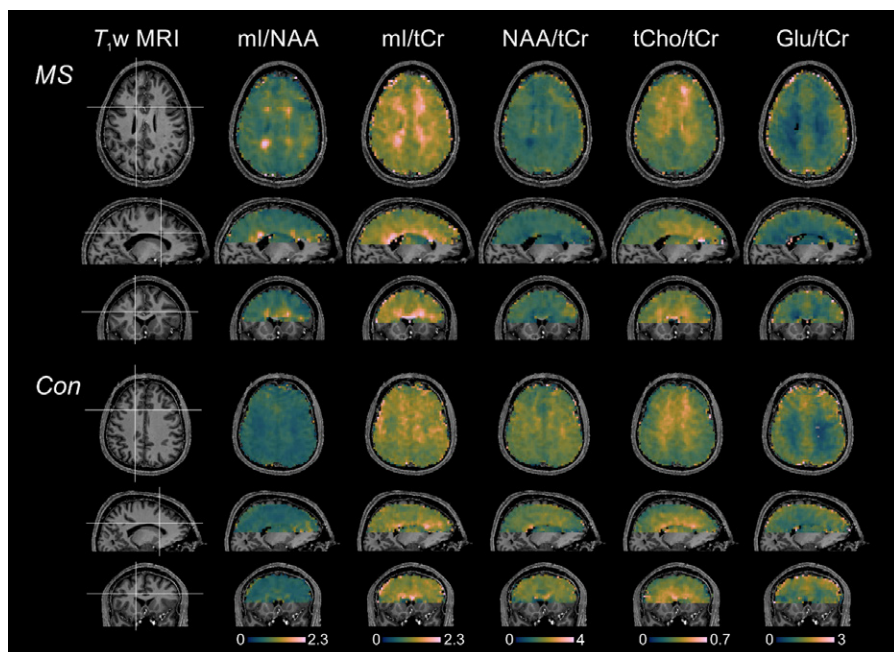
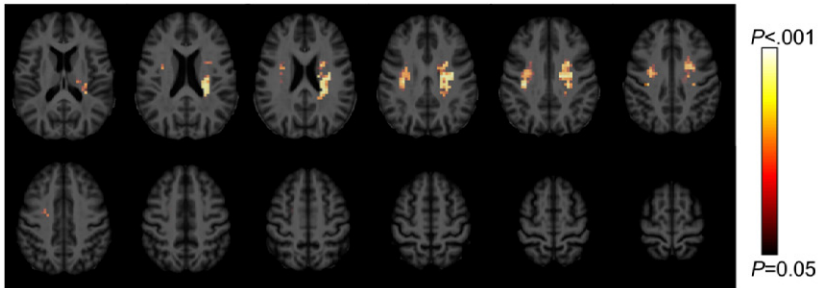
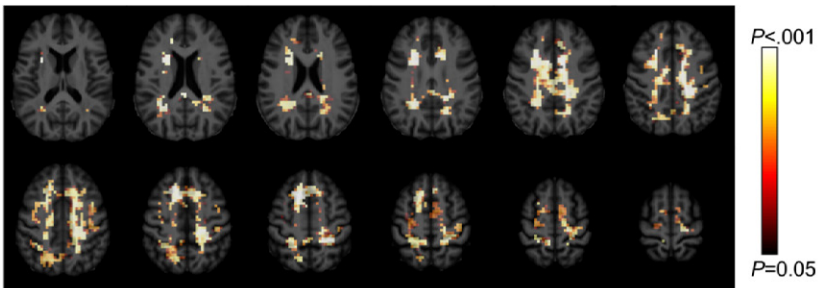


Figure 1

A. Elevated mI/tCr



B. Reduced NAA/tCr



C. lesion probability map

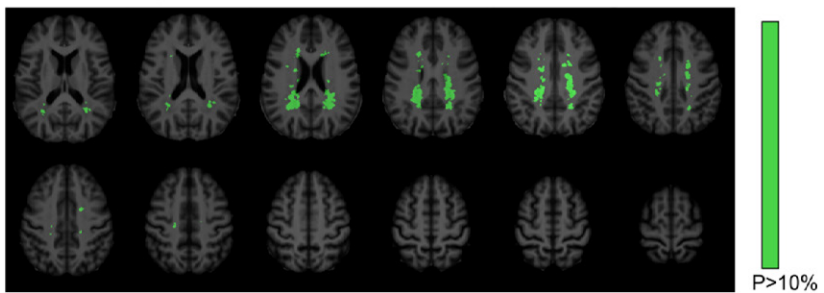
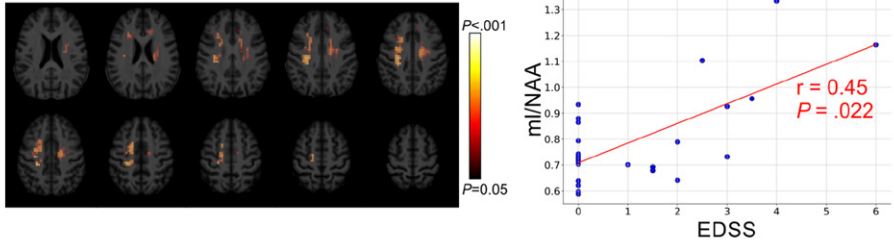


Figure 2

$$mI/NAA = f(EDSS)$$



**Figure 3**

### Picture description

**Figure 1:** Sample metabolic maps obtained with 3D-MR spectroscopic imaging from one multiple sclerosis (MS) and one age-matched healthy control (Con). Metabolic abnormalities associated with MS can be seen particularly on myo-inositol/total creatine (mI/tCr), N-acetylaspartate/total creatine (NAA/tCr) and myo-inositol/N-acetylaspartate (mI/NAA) maps.

**Figure 2:** Statistical mapping revealed clusters of elevated myo-inositol to total creatine (mI/tCr) (A) and reduced N-acetylaspartate to total creatine (NAA/tCr) in MS patients relative to controls. Metabolic abnormalities were partially co-localized with WM lesions (C), but also more widespread across brain, exceeding lesional pathology.

**Figure 3:** Clusters of positive correlations between myo-inositol to N-acetylaspartate (mI/NAA) and clinical disability (EDSS) in MS patients and Spearman's rank correlation within significant clusters.

## High Permittivity Dielectric Metasurface Enhances Transmission Efficiency of a Surface Loop at 7T

Nandita Saha<sup>1,2</sup>, Bilguun Nurzed<sup>1,3</sup>, Santosh Kumar Maurya<sup>4</sup>, Rita Schmidt<sup>4</sup>, Thoralf Niendorf<sup>1,2</sup>

<sup>1</sup>Max-Delbrück-Center for Molecular Medicine in the Helmholtz Association (MDC), Berlin Ultrahigh Field Facility (B.U.F.F.), 13125 Berlin, Germany

<sup>2</sup>Charité—Universitätsmedizin Berlin, Experimental and Clinical Research Center (ECRC), A Joint Cooperation between the Charité Medical Faculty and the Max-Delbrück Center for Molecular Medicine in the Helmholtz Association, 13125 Berlin, Germany

<sup>3</sup>Chair of Medical Engineering, Technische Universität Berlin, 10623 Berlin, Germany

<sup>4</sup>Department of Brain Sciences, Weizmann Institute of Science, Rehovot 7610001, Israel

### Purpose

Ultra-high field (UHF,  $B_0 \geq 7T$ ) MRI, offers superior signal-to-noise ratios and local surface transceive (TxRx) RF coils enable enhanced tissue excitation<sup>[1,2]</sup>. Metasurfaces (MS), which are planar versions of metamaterials, are conceptually appealing for manipulating RF wave propagation to enhance B-field uniformity, depth penetration, and MRI sensitivity<sup>[1-7]</sup>. Recognizing this opportunity, our work examines signal intensity gain at 7T using a high permittivity dielectric (HPD) MS in conjunction with an one-channel TxRx loop coil (1L).

### Methods

The HPD-MS and 1L were designed in CST microwave studio 2020 [Fig. 1a,b]. Bench measurements were done with an 8-channel network analyzer (VNA) (Rohde & Schwarz). The HPD-MS (size:16x11x0.7cm<sup>3</sup>) comprises 6x5 array of uniformly spaced copper shortstrips on an HDP substrate [Fig. 1b]. The HDP ( $\epsilon_r=164$ ) substrate of the MS is composed of BaTiO<sub>3</sub> (50g) + CaTiO<sub>3</sub> (30g) + H<sub>2</sub>O distilled (10ml). The 1L (size:10x10x0.05cm<sup>3</sup>) incorporated three distributed fixed capacitors (C) was tuned and matched to 297.2MHz using capacitive tuning (C<sub>r</sub>), matching (C<sub>m</sub>) networks [Fig. 1a]. The feeding port of the 1L was connected to the transmit path of the TxRX switch (Stark Contrast Erlangen, Germany). For performance evaluation, MR images were obtained using a rectangular phantom (45x27x10cm<sup>3</sup>) ( $\epsilon_r=58$ ;  $\sigma=0.77S/m$ ) filled with water, PVP, and salt for 1L with and without MS. MRI experiments were performed using Siemens 7.0 T (MAGNETOM, Siemens Healthineers, Germany). A gradient echo sequence (FLASH) was used for MRI with spatial resolution = 4x4x4 mm<sup>3</sup>; TE/TR=2.46/440ms; Flip angle= 90°; FoV= 220x320 mm; transmitter voltage =200V.

## Results

Our VNA measurements revealed a resonant mode at 297.2MHz with the HPD-MS placed on the phantom [Fig. 1b]. Fig. 1c shows phantom data obtained from 2D GRE MRI. The 1L+MS setup yielded 108%, 179% higher mean signal intensity and improved FoV coverage for central transversal, sagittal slices versus the 1L setup. To summarize, constructive redistribution of the magnetic field facilitated by the HPD-MS benefits signal intensity enhancement.

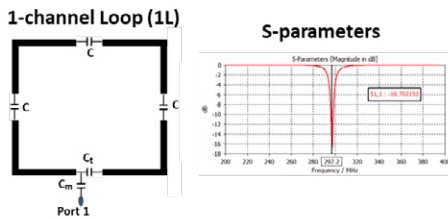
## Conclusion

Our results demonstrate that HPD-MS enhances the transmission efficiency of a one-channel surface loop coil at 7T. The benefit of this MS is that the eigenmode properties can be customized by adjusting shortstrip's size, periodicity, or structure placement relative to the imaging location for enhanced transmit efficiency and field homogeneity.

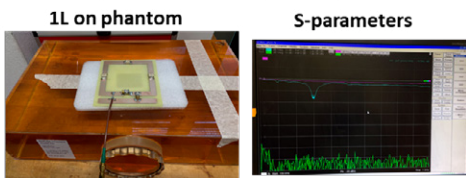
## References

1. Weinberger O; PLoS One. 2016 Sep6;11(9):e0161863. doi: 10.1371/journal.pone.0161863.
2. Lakshmanan K; Magn Reson Eng. 2020;2020:8886543. doi: 10.1155/2020/8886543.
3. Alipour, A; Med Phys. 2023; 1-13. <https://doi.org/10.1002/mp.16801>.
4. Schmidt R; ACS Appl Mater Interfaces. 2017 Oct 11;9(40):34618-34624. doi: 10.1021/acsami.7b06949.
5. Webb A; MAGMA. 2022Dec;35(6):875-894. doi: 10.1007/s10334-022-01007-5.
6. Maurya, S.K.; Sensors 2024, 24, 2250. <https://doi.org/10.3390/s24072250>

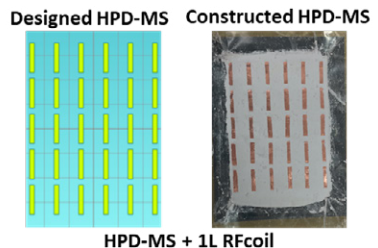
### (a) Simulation setup of loop coil



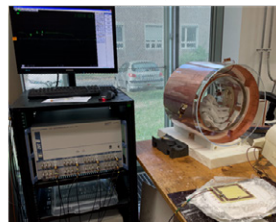
### Experimental setup of loop coil



### (b) High-permittivity dielectric metasurface (HPD-MS)



### HPD-MS + 1L RFcoil



### (c) GRE scan of phantom

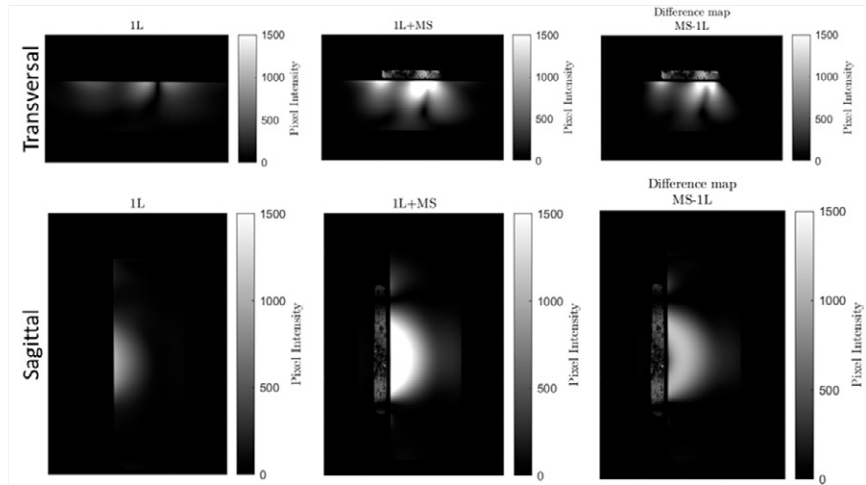


**Figure 1**

- (a) Schematic of 1-channel loop (1L) coil. The 1L was tuned and matched to a resonant frequency of 297.2MHz for 7T ( $S_{11} = -16.4\text{dB}$ ). Experimental setup of the 1L placed on a rectangular phantom ( $45 \times 27 \times 10 \text{ cm}^3$ ) ( $\epsilon_r = 58$ ;  $\sigma = 0.77\text{S/m}$ ) mimicking muscle tissue for bench measurement. Three fixed ceramic capacitors of (C) 4.7pF and tuning (Ct), matching (Cm) trimmer capacitors (1–23 pF) were soldered directly onto the surface. The 1L was tuned and matched to resonant frequency of 297.2MHz ( $S_{11} = -17\text{dB}$ ) of 7T.
- (b) The HPD-MS ( $16 \times 11 \times 0.7 \text{ cm}^3$ ) comprises a  $6 \times 5$  array of copper short strips 2cm apart on an HDP substrate ( $\epsilon_r = 164$ ).
- (c) MRI through rectangular phantom acquired with a 2D gradient echo sequence (FLASH). Signal intensity were assessed for the central transversal, sagittal slice through the phantom for 1L and 1L+MS setup.

## Monitoring myocardial T2\* transient change in HCM – a mouse study

Shahriar Shalika<sup>1</sup>, Oumaima Laghzali<sup>1,2,3</sup>, Siqin Liu<sup>1,2,3</sup>, Sandra Lehmann<sup>1</sup>, Sonia Waiczies<sup>1,7</sup>, Lucie Carrier<sup>4,5</sup>, Hsin-Jung Yang<sup>6</sup>, Thoralf Niendorf<sup>1,2,7</sup>, and Min-Chi Ku<sup>1,2</sup>

<sup>1</sup>Berlin Ultrahigh Field Facility (B.U.F.F.), Max Delbrück Center for Molecular Medicine in the Helmholtz Association, Berlin, Germany

<sup>2</sup>DZHK (German Centre for Cardiovascular Research), partner site Berlin, Germany

<sup>3</sup>Charité-Universitätsmedizin Berlin, Berlin, Germany

<sup>4</sup>Department of Experimental Pharmacology and Toxicology, University Medical Center Hamburg-Eppendorf, Hamburg, Germany

<sup>5</sup>DZHK (German Centre for Cardiovascular Research), partner site Hamburg/Kiel/Lübeck, Germany

<sup>6</sup>Biomedical Imaging Research Institute, Cedars-Sinai Medical Center, Los Angeles, CA, USA

<sup>7</sup>Experimental and Clinical Research Center (ECRC), a joint cooperation between the Charité Medical Faculty and the Max-Delbrück Center for Molecular Medicine, Berlin, Germany

### Introduction

Myocardial pathological changes, including hemorrhage, oxygenation, and fibrosis, can be detected by variations in myocardial T2\* [1]. This intrinsic tissue parameter is crucial for understanding the pathophysiology of cardiomyopathies and heart failure.

Standard gated Multi-Gradient-Echo (MGE) T2\* imaging is susceptible to unsuccessful gating due to disruptions in ECG signals of animal models with high heart rates ranged between 400 to 600 bpm. Detailed examination of transient T2\* changes throughout the cardiac cycle necessitates cinematic T2\*-mapping to differentiate the oxygenation changes and fibrosis happening in hypertrophic cardiomyopathy (HCM) [2, 3]. To address this, we developed a retrospective gating technique for MGE data acquisition, utilizing pulse oximetry signals to capture heart activity without the need for ECG. We evaluated the performance of our method on T2\* phantoms and simulated its robustness against different confounding situation. An in vivo study was performed on a HCM mouse model investigating its myocardial T2\* changes throughout the cardiac cycle.

### Method

We used an HCM mouse model carrying the mybpc3 gene mutation represent the human HCM. In total, 5 mybpc3-KI mice and 5 wild-type control mice (Table 2) were [KMC1] used in accordance with local animal welfare guidelines. Figure 1 illustrates the data collection and reconstruction framework. The MGE data were collected continuously in mid-level short axis (SAX)-view of mice heart at Bruker 9.4T small

animal MRI. To mitigate the potential impact of local magnetic field inhomogeneity on T2\*, 2nd-order shimming was applied with a region of interest covering the heart. Retrospective ECG-gating approach was applied and the data sorted into 10 cardiac phases with a complex average in k-space domain [4, 5]. CINE T2\*-maps were obtained from a monoexponential fit of the T2\* decay. Mean T2\* were measured in the region free of off-resonance (Figure 4A). To examine the binning performance, a phantom study was performed with 6 representative iron concentrations: 0.75, 1, 2, 3, 4 and 5 $\mu$ l ferumoxytol (containing 0.03 g/ml iron) per 1ml distilled water (see Figure 2A). Two sets of image reconstruction were applied on the same rawdata for comparison. The phase-encoding ordering is linear sequential cartesian with 7 echo images (More details is provided in Table 1). To assess the method's robustness, several simulations was performed with different cardiac phase, cardiac duration variability and number of repetitions (averages) on the phantom.

## Results

Using phantoms, T2\* maps derived from both the reference and retrospective binning scheme, exhibited high image quality and demonstrated similar T2\* values for each iron concentration (Figure 2A). Figure 2B shows Bland-Altman and correlation plots indicating strong consistency between the retrospective binning and the reference method, with R2=1 and ICC1. Figure 3 shows the simulation performance of retrospective binning method on calculated T2\* map. The simulation was performed by varying heart period, number of cardiac phase and repetition (average) parameters. Heart rate was simulated to provide the Triggering information for binning. In Figure 3B, the highlighted column represents a static acquisition without binning, which serves as the reference value for comparison. Increased the number of averages improves the SNR, making T2\* values more accurate and aligning them with the reference value as the repetition count reaches 300. In Figure 4, mean myocardial T2\* was calculated for each mouse across all cardiac phases. Figure 4 shows the average of mean T2\* curve in the region of interest for WT and mybpc3-KI mouse. Myocardial T2\* was significantly increased in the HCM model versus control mice (T2\*(KI) = 13.67  $\pm$  2.21 ms vs T2\*(WT) = 10.81  $\pm$  2.43 ms).

## Discussion

These results demonstrate the feasibility of free-running T2\* mapping in mouse hearts using a retrospective gating approach. The differences in myocardial T2\* between WT and HCM mice provide a new metric for tissue characterization, offering valuable insights into myocardial pathophysiology and improving the ability to predict and intervene in disease progression. Future work will focus on expanding these techniques to other disease models and human studies, refining the sensitivity and specificity of T2\* measurements, and exploring their potential for early

diagnosis and personalized treatment strategies for heart disease. Additionally, validation through histological analysis and investigation of underlying mechanisms will be pursued.

### Conclusion

Continuous acquisition with retrospective gating, free breathing, and cardiac motion-resolved  $T_2^*$  mapping throughout the entire cardiac cycle enables the detection of myocardial  $T_2^*$  differences across various genotypes and phenotypes. These  $T_2^*$  variations serve as a potential marker, offering insights into different stages of myocardial pathophysiology and enhancing the prediction and early intervention of disease progression.

### References

- [1] M. Gastl *et al.*, "Cardiovascular magnetic resonance  $T_2^*$  mapping for structural alterations in hypertrophic cardiomyopathy," *European journal of radiology open*, vol. 6, pp. 78-84, 2019.
- [2] T. Huelnhagen *et al.*, "Myocardial effective transverse relaxation time  $T_2^*$  is elevated in hypertrophic cardiomyopathy: A 7.0 T magnetic resonance imaging study," *Scientific Reports*, vol. 8, no. 1, p. 3974, 2018.
- [3] S. L. O. Laghzali, J. Periquito, A. Pohlmann, L. Carrier, T. Niendorf, S. Waiczies and M. Ku, "Full cardiac cycle coverage  $T_2^*$  mapping detects early myocardial changes in hypertrophic cardiomyopathy," *International Society of Magnetic Resonance in Medicine (ISMRM)*, 2023.
- [4] O. L. Shahriar Shalika, Siqin Liu, Andreas Pohlmann, Joao dos Santos Periquito, Sonia Waiczies, Thoralf Niendorf, Min-Chi Ku, "Improving Cardiac Phase-Resolved  $T_2^*$ -Mapping of the Murine Heart: Artifact Reduction and Enhanced Accuracy," *International Society of Magnetic Resonance in Medicine (ISMRM)*, 2024.
- [5] M. K. S. Lehmann, A. Pohlmann, J. Periquito and T. Niendorf, "Flexible and efficient cardiac cine magnetic resonance imaging in fast beating heart," presented at the International Society of Magnetic Resonance in Medicine (ISMRM), 2020.

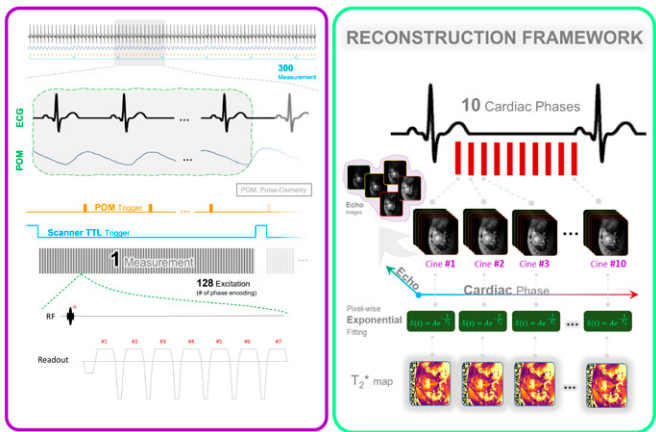
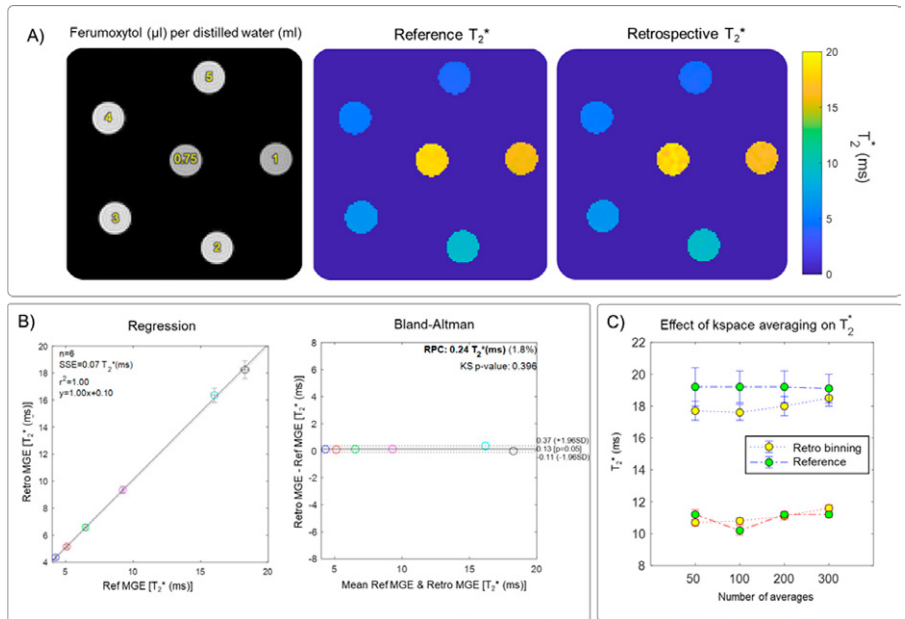
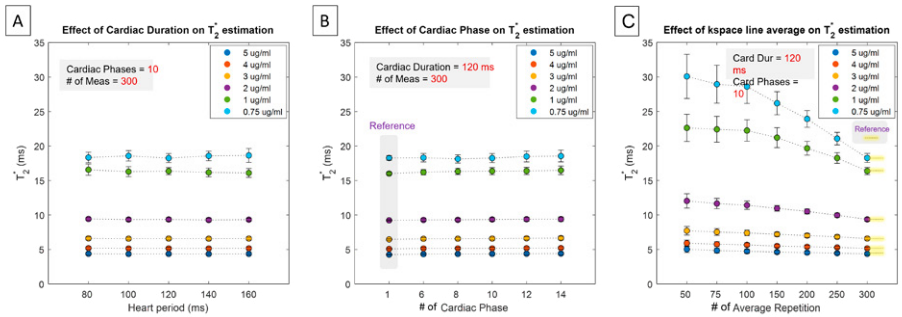


Figure 1



**Figure 2**



**Figure 3**

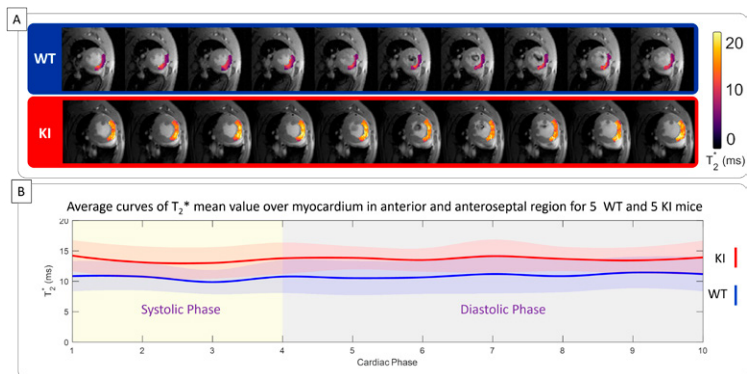


**Figure 4**

Parameters	<i>In vivo/T<sub>2</sub>* Phantom</i>
TR (ms)	14
First TE (ms)	1.5
Echo Spacing (ms)	1.6
# of Echo Images	7
FOV (mm) - Slice Thickness	30x30 - 0.8
Matrix Size	128x128
Excitation flip angle (°)	10°
Receiver bandwidth (kHz)	133
# of Measurements*	300
Scan time	10m6s0ms
Sequence	MGE- monopolar
Nominal Average**	27
Cardiac Phase	10

\* Each measurement comprises of a whole 2D acquisition.

\*\* The nominal average is determined by the quality of triggering

Parameters	WT	HCM
Background	C57BL/6J	C57Bl/6*
Number (female)	5 (2)	5 (3)
Age (weeks old)	9.9 +- 0.9	8.4 +- 2.1

\* This model carries the mybpc3 gene mutation, which impacts the cardiac myosin-binding protein C (cMyBP-C), reflecting key features of the human condition.

**Table 1**

**Table 2**

### Picture description

**Figure 1.** Data Acquisition and Reconstruction scheme used for whole cardiac cycle T<sub>2</sub>\*-mapping of the mouse heart. MRI data acquisition is performed continuously in synchronization with the pulse-oximetry and with the scanner's TTL trigger signal. Following data collection, retrospective sorting based on recorded signals is performed. Each k-space line is assigned to the corresponding cardiac phase and then averaged to yield 10 cardiac phases, each with 7 echoes. T<sub>2</sub>\* maps are generated via pixel-wise mono-exponential fitting of the T<sub>2</sub>\* signal decay.

**Figure 2.** T<sub>2</sub>\* phantom study and qualitative comparison and quantitative analysis with reference value. A) Qualitative comparison of T<sub>2</sub>\* map. An exemplary first echo image (TE= 1.5) of six iron concentrations reconstructed by the retrospective binning approach together with T<sub>2</sub>\* maps of the phantom obtained for conventional MGE and retrospective binning MGE. B) Regression and Bland-Altman analysis. The retrospective binning approach shows strong correlation with the reference method, as indicated by R<sub>2</sub>. The dotted line shows identity line, while the solid line illustrates the linear regression fitting. Bland-Altman plot also depict the comparison of the reference method with the retrospective binning approach. The dashed lines indicate a confidence level of 95%, while the continuous lines depict the average percentage variances.

**Figure 3.** Simulation result showing retrospective binning reconstruction performance as a function of heart period, number of cardiac phase and repetition (average) on T<sub>2</sub>\* estimation on the phantom data described in Figure 2 triggered by simulated heartrate. A) Robustness of the proposed binning method against heart period variation within a range that can occur in actual in vivo experiments. B) The number of cardiac phases was also analysed as a metric to demonstrate the performance of the reconstruction. A total cardiac phase of 1 represents a static acquisition without binning, which serves as the reference value for comparison. C) As the average increases, the T<sub>2</sub>\* values converge toward the reference value at a repetition number of 300. The average is performed in k-space domain.

**Figure 4.** In vivo myocardium T<sub>2</sub>\* measurement covering the whole cardiac cycle in wt and in HCM mice in the region of no off-resonance artifact. A) Representative regional T<sub>2</sub>\* maps superimposed to anatomic images obtained for 10 cardiac phases for a male wt control mice (top) and for a female mybpc3-ki mice (bottom). B) Comparison of T<sub>2</sub>\* between wt controls and mybpc3-ki HCM mice reveals elevated T<sub>2</sub>\* values in the HCM mice across all cardiac phases (n=10 mice). There is a T<sub>2</sub>\* variation across the cardiac cycle

**Table 1:** Scan parameters used for the phantom and for the in vivo study.

**Table 2.** In vivo study statistics

## In Vivo Monitoring of Renal Tubule Volume Fraction During Acute Tubular Pressure Increase Using Dynamic $T_2$ Mapping

Ehsan Tasbihi<sup>1,2</sup>, Thomas Gladytz<sup>1</sup>, Jason M. Millward<sup>1,5</sup>, João S Periquito<sup>1</sup>, Ludger Starke<sup>1,3</sup>, Sonia Waiczies<sup>1,5</sup>, Kathleen Cantow<sup>4</sup>, Erdmann Seeliger<sup>4</sup>, Thoralf Niendorf<sup>1,5</sup>

1 Berlin Ultrahigh Field Facility (B.U.F.F.), Max Delbrueck Center for Molecular Medicine in the Helmholtz Association, Berlin, Germany

2 Charité – Universitätsmedizin Berlin, Berlin, Germany

3 Hasso Plattner Institute for Digital Engineering, University of Potsdam, Germany

4 Institute of Translational Physiology, Charité – Universitätsmedizin Berlin, Berlin, Germany

5 Experimental and Clinical Research Center, a joint cooperation between the Charité Medical Faculty and the Max Delbrück Center for Molecular Medicine, Berlin, Germany

### Introduction

The increasing incidence of kidney diseases is a global concern. Current diagnostic tools and therapies for renal disease are inadequate. Changes in the renal tubule volume fraction (TVF) may serve as a marker for kidney disease and provide a better understanding of renal (patho-)physiology<sup>1</sup>.  $T_2$  mapping, an established MRI technique, can quantify changes in tissue water fraction noninvasively<sup>2</sup>. This study is the first report on in vivo assessment of relative changes in the renal tubular volume fraction as a (patho) physiological metric and uses  $T_2$  mapping in conjunction with bi-exponential analysis of the  $T_2$  decay to determine relative changes TVF during acute renal pelvis/tubular pressure increase, which is a clinically relevant intervention.

### Methods

Tubular fluid, which originates from ultrafiltration in the glomeruli, has a substantially longer  $T_2$  compared to the renal parenchyma. Therefore, the tubular contribution to the signal should be separable from the parenchyma signal by nonlinear least squares regression. The numerical solution for multi-exponential decomposition was done using MATLAB functions. The algorithm was evaluated using synthetic data simulations and measurements in phantoms. Since in vivo experiments are always limited by the constraints of acquisition time, spatial resolution and SNR, we evaluated the multi-exponential decomposition approach in simulations using a broad range of conditions of  $T_2$  mapping. A phantom was designed to mimic realistic changes of TVF in the rat kidney (Fig.1). Water was doped with  $MnCl_2$  and  $CuSO_4$  to achieve  $T_1$  and  $T_2$  times similar to the tubular fluid and the renal parenchyma. This was followed by a proof-of-principle demonstration using in vivo data obtained during a transient increase of renal pelvis and tubular pressure in rats (Fig.2). MRI data were acquired on a 9.4 Tesla small animal MR system (Bruker Biospec 94/20,

Bruker Biospin, Ettlingen, Germany) using a linear radiofrequency (RF) volume resonator and a 4-channel surface RF coil array tailored for rats (Bruker Biospin). For  $T_2$  mapping a multi-echo spin-echo technique (TR=500ms, number of echoes=13, first TE=6.4ms, interecho time  $\Delta TE=6.4$ ms, number of averages=1, acquisition=58s) was employed. For  $T_2$  mapping a mid-coronal oblique slice was acquired (in-plane spatial resolution=(226×445)  $\mu\text{m}^2$ , FOV=(38.2×50.3)  $\text{mm}^2$ , matrix size=169×113, slice thickness=1.4mm).

## Results

Figure 3 demonstrates the impact of echo spacing ( $\Delta TE=5-50$ ms) and SNR=5 to 600 on the TVF estimation. Using a high accuracy imaging protocol (TR=4s, number of echoes=13, first TE=15ms,  $\Delta TE=15$ ms, number of averages=3,  $t_{\text{acquisition}}=47$ min), our approach achieved a high accuracy on the phantom. Since in vivo experiments are limited by acquisition time constraints we developed an accelerated protocol tailored for in vivo  $T_2$  mapping of the rat kidney (TR=500ms, number of echoes=13, first TE=6.4ms, inter-echo time  $\Delta TE=6.4$ ms, number of averages=1,  $\alpha_{\text{refocusing pulse}}=180^\circ$ ,  $t_{\text{acquisition}}=58$ s), which resulted in an accuracy of MAE<3%. Fig. 1C shows a  $T_2$  map obtained for the phantom. The histogram (Fig. 1D) shows the  $T_2$  distribution for the selected ROI. Changes in the ratio of the volume fraction of the two compartments were achieved by changing the ROI size. Fig. 1E shows TVF measured for the high accuracy protocol and for the accelerated protocol customized for the in vivo study. Fig. 4 shows representative quantitative TVF maps obtained for baseline, transient pelvis and tubular pressure increase, and recovery. Transiently increasing pressure in the renal pelvis and tubules induced significant changes in TVF in renal compartments:  $\Delta TVF_{\text{cortex}}=5.2\%$ ,  $\Delta TVF_{\text{outer medulla}}=2.6\%$ , and  $\Delta TVF_{\text{inner medulla}}=-14.2\%$  (Fig.5).

## Discussion

This is the first report on in vivo estimation of the physiological metric renal tubular volume fraction. We demonstrate the feasibility of dynamic parametric mapping of the MRI relaxation time  $T_2$  for TVF cartography and for monitoring physiological changes in the TVF. For the first time, we represent parametric maps of TVF obtained under normal conditions and upon increased pelvis and tubular pressure, which is a clinically relevant intervention. Future in vivo validation of our MRI approach to TVF assessment with intravital microscopy, i.e. for quantitative comparison of changes in the vascular and renal tubular compartments with those observed by and  $T_2$ , is warranted. In this work, our MRI-based monitoring was focused on retrospective assessment of changes in TVF during an acute pathophysiological scenario. Future steps will include prospective and real-time application of  $T_2$  decomposition and TVF measurement, integrating our decomposition analysis directly into the image reconstruction and post-processing pipeline of the MR scanner.

## Conclusion

Our investigations have the potential to help uncover the mechanisms leading to acute kidney injury and progression to chronic kidney disease. Monitoring of relative changes in renal TVF *in vivo* using dynamic parametric MRI provides a potential rapid, noninvasive marker for kidney disease. This approach will be invaluable for gaining a better mechanistic understanding of renal (patho-)physiology.

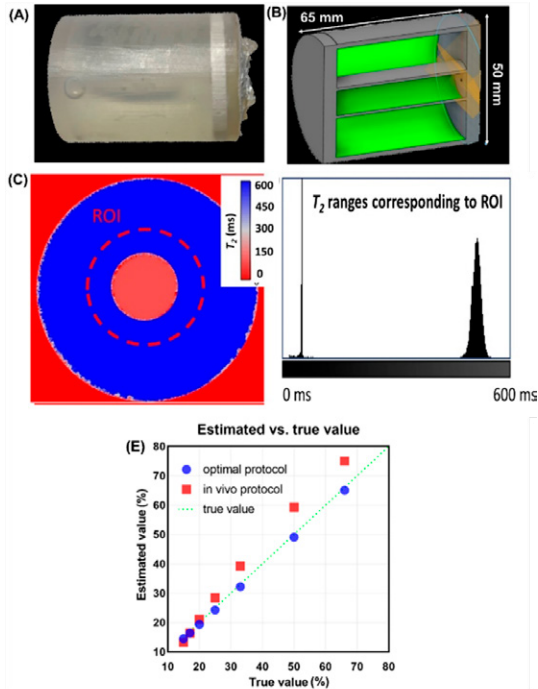


Figure 1

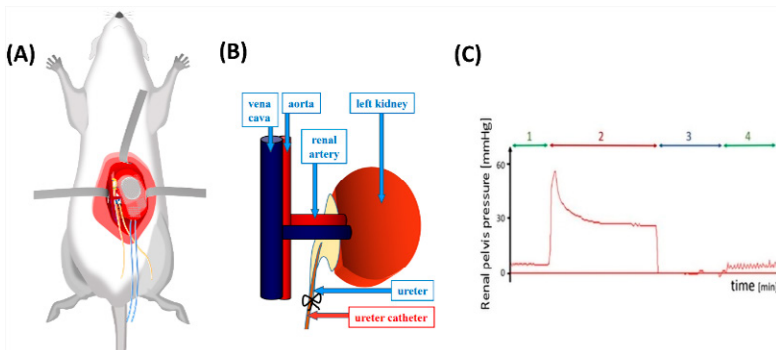


Figure 2

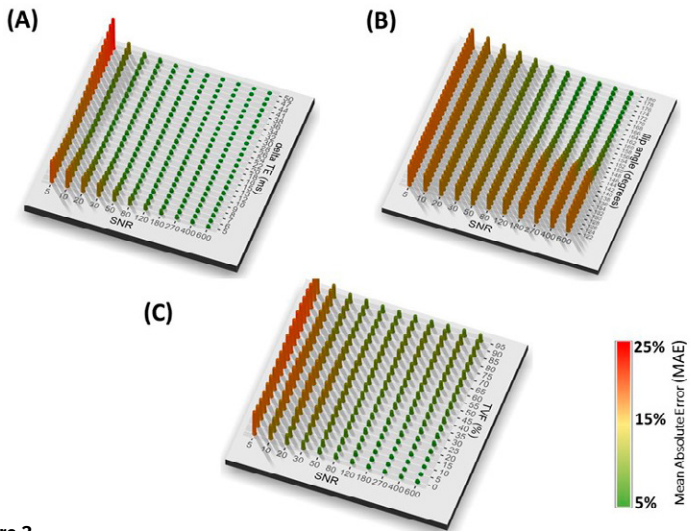


Figure 3

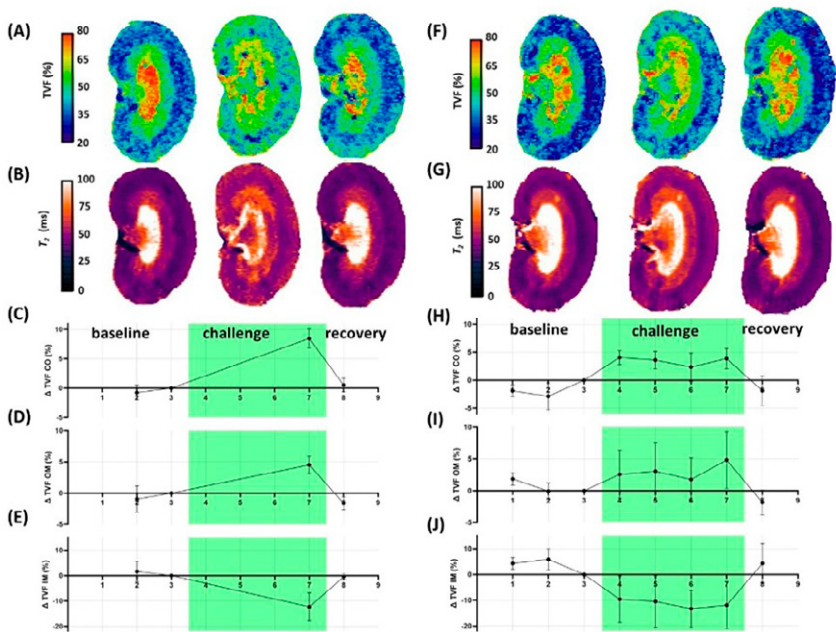
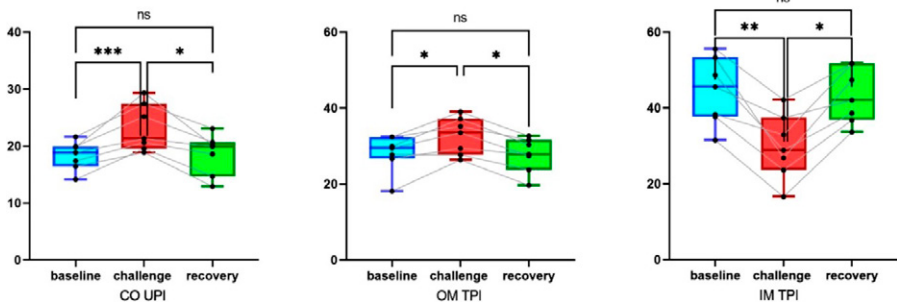


Figure 4



**Figure 5**

**Picture description**

**Figure 1:** (A). Photograph of the phantom. (B). Schematic view of the phantom (C). shows the reconstructed T2 map in milliseconds of the custom-built T1- T2 phantom (scan parameters: T2- (MESE), 13 echoes, echo-spacing=6.4ms, TR=1s; scan time 16 s) (D). an exemplary ROI selection and the histogram shows T2 distribution corresponding to the selected ROI. E. Evaluation of the assessment of the volume fraction with decomposition of parametric T2 in a mechanical phantom using the optimal protocol derived from the simulations (true value, TR = 4 s, number of echoes = 15, first TE = 15 ms, interecho time  $\Delta TE = 15$  ms, number of averages = 3) and the protocol adapted for the in vivo measurements (estimated value, TR = 1 s, number of echoes = 13, first TE = 6.4 ms, interecho time  $\Delta TE = 6.4$  ms, number of averages = 1,  $t_{\text{acquisition}} = 58$  s). The correlation coefficient between the estimated and the true value is: 0.997.

**Figure 2:** Illustration of the methods utilized for remotely controlled brief increases in renal pelvis and tubular pressures. (A) Schematic view depicting the relevant positions and fixations of probes. (B) Catheter placed in the left ureter and connected via a catheter (length about 1.5 m) to a container filled with isotonic saline. Elevating the container 41 cm above the level of the rats' kidneys increased pelvis and tubular pressures by about 30 mm Hg. (C) Pressure trace obtained for the renal pelvis of a rat (pressure transducer: DT-XX, Viggo-Spectramed, Swindon, UK; amplifier & acquisition: TAM-A Plugsys & HAEMODYN, Hugo Sachs Elektronik, March, Germany) recorded (1) during baseline control conditions (green), (2) during pressure increase achieved by injection of saline fluid via the ureteral catheter (red), (3) following disconnection of the catheter to obtain zero pressure for calibration of the pressure measurement (dark blue) and (4) during another control measurement (green). Note that the oscillations observed during first (1) and, even enlarged, during second control (4) represent the spontaneous peristaltic contractions of the ureter.

**Figure 3:** A. Representative example of Mean Absolute Error (MAE) calculated after analyzing the  $T_2$  decay of the synthetic data with bi-exponential analysis. The table shows the impact of SNR, and the echo spacing on accuracy of TVF estimation. Other simulation parameters were  $T_{2\text{ long}}=500\text{ms}$ ,  $T_{2\text{ short}}=50\text{ms}$ ,  $T_{1\text{ long}}=2800\text{ms}$ ,  $T_{1\text{ short}}=1500\text{ms}$ , NumOfEchoes= 13, flipAng=180°. Numbers are in percentage. B: Representative example of Mean Absolute Error (MAE) calculated after analyzing the  $T_2$  decay of the synthetic data with bi-exponential analysis for a variety flip angle and SNR. Other simulation parameters were  $T_{2\text{ long}}=500\text{ms}$ ,  $T_{2\text{ short}}=50\text{ms}$ ,  $T_{1\text{ long}}=2800\text{ms}$ ,  $T_{1\text{ short}}=1500\text{ms}$ , NumOfEchoes= 13, esp=6. Numbers are in percentage. C. Representative example of Mean Absolute Error (MAE) calculated after analyzing the  $T_2$  decay of the synthetic data with bi-exponential analysis for a variety of TVF and SNR of simulation parameters: other parameters were  $T_{2\text{ long}}=500\text{ms}$ ,  $T_{2\text{ short}}=50\text{ms}$ ,  $T_{1\text{ long}}=2800\text{ms}$ ,  $T_{1\text{ short}}=1500\text{ms}$ , NumOfEchoes= 13, flipAng=180°. Numbers are in percentage.

**Figure 4:** Time courses during renal pelvis/tubular pressure increase. (A, B) Exemplary TVF and  $T_2$  maps obtained for a rat kidney in vivo of the first subgroup (n=3). Time course of the TVF changes (mean  $\pm$  SEM) for (C) cortex (CO), (D) outer medulla (OM), and (E) inner medulla (IM) before the intervention (baseline), during the intervention (green area), and during recovery acquired for the first subgroup n=3. (F-J) Time courses during renal pelvis/tubular pressure increase, obtained for the second sub-group (n=4). Exemplary

TVF and  $T_2$  maps obtained for a rat kidney in vivo (F,G). Time course of the TVF changes (mean  $\pm$  SEM) for (H) cortex (CO), (I) outer medulla (OM), and (J) inner medulla (IM) before the intervention (baseline), during the intervention (green area), and during recovery acquired for the second subgroup  $n=4$ .

**Figure 5:** Box-and-whisker plots showing changes of tubular volume fraction (TVF) during pelvis/ureter pressure increase. TVF was significantly increased in the kidneys' cortex and outer medulla during intervention ( $p=0.0005/p=0.0162$ ; Dunn's multiple test vs. baseline). TVF reduction was significant for inner medulla ( $p=0.0075$ ; Dunn's multiple test vs. baseline). The box-and-whisker plots display the first and third quartiles, with the line within the box representing the median value. The whiskers denote the minimum and maximum values. Volumes were examined by non-parametric multicomparison, comparing TVF among all three conditions using Dunn's multiple test for multiple comparisons ( $n=7$  subjects).

## Synopsis

**Motivation:** The increasing incidence of kidney diseases is a global concern and current biomarkers are inadequate. Changes in renal tubule volume fraction (TVF) may serve as a rapid biomarker for kidney disease and provide a better understanding of renal (patho-)physiology.

**Goal(s):** This study aims to measure TVF in in vivo rat kidney during acute tubular pressure increase

**Approach:** This study uses the amplitude of the long T2 component as a surrogate for TVF in rats, by applying multiexponential analysis of the T2 driven signal decay

**Results:** The results demonstrate that our approach is promising for research into quantitative assessment of renal TVF in in vivo applications.

**Impact:** This is the first report on in vivo assessment of relative changes in the renal TVF, which provides a potential rapid, noninvasive marker for kidney disease. This approach will be invaluable for gaining a better mechanistic understanding of renal (patho-)physiology.

## Acknowledgement

This work was funded in part by the German Research Foundation (394046635, SFB 1365, and RENOPROTEC-TION, to Thoralf Niendorf, Erdmann Seeliger, Sonia Waiczies, Thomas Gladytz, and Kathleen Cantow). The authors thank A. Pohlmann (Max-Delbrueck Center for Molecular Medicine in the Helmholtz Association, Berlin, Germany), and A. Anger, and B. Flemming (Institute of Translational Physiology, Charité–Universitätsmedizin, Berlin, Germany) for technical and other support. Open Access funding enabled and organized by Projekt DEAL

## References

- [1] Toward Assessment of Renal Tubule Volume Fraction in Rat Kidney Using Decomposition of Parametric T2. Tasbihi E., Gladytz T., Starke L., Millward J., Seeliger E., and Niendorf T. ISMRM 2023
- [2] Continuous diffusion spectrum computation for diffusion-weighted magnetic resonance imaging of the kidney tubule system. Quantitative Imaging in Medicine and Surgery. Periquito, J. S., Gladytz, T., Millward, J. M., Delgado, P. R., Cantow, K., Grosenick, D., ... & Niendorf, T. 3098, s.l. : Quantitative Imaging in Medicine and Surgery, 2021, Vol. 11

# Sponsors

The organizers gratefully acknowledge the symposium's sponsors who provided kind contributions to foster science and educational activities.



[www.bruker.com](http://www.bruker.com)



[www.siemens-healthineers.com](http://www.siemens-healthineers.com)



[www.rricorp.com](http://www.rricorp.com)



[www.nvision-imaging.com](http://www.nvision-imaging.com)



[www.united-imaging.com](http://www.united-imaging.com)